

REPORT DOCUMENTATION PAGE

AFRL-SR-AR-TR-04-

Public reporting burden for this collection of information is estimated to average 1 hour per response, including the time for reviewing instructions, searching the collection of information. Send comments regarding this burden estimate or any other aspect of this collection of information, including suggestion Operations and Reports, 1215 Jefferson Davis Highway, Suite 1204, Arlington, VA 22202-4302, and to the Office of Management and Budget, Paperwork

1. AGENCY USE ONLY (Leave blank)	2. REPORT DATE	3. REPORT	.0229
		Final Technical Report (15 Nov 99 - 31 Dec 02)	
4. TITLE AND SUBTITLE		5. FUNDING NUMBERS	
Mixing and Noise in High Speed Axisymmetric Jets		F49620-00-1-0023 2307/AX 61102F	
6. AUTHOR(S)		8. PERFORMING ORGANIZATION REPORT NUMBER	
M.. Samimy, J. Hileman, and E. Caraballo			
7. PERFORMING ORGANIZATION NAME(S) AND ADDRESS(ES)		9. SPONSORING/MONITORING AGENCY NAME(S) AND ADDRESS(ES)	
Ohio State University Dept of Mechanical Engineering Columbus, OH 43210		AFOSR/NA 4015 Wilson Blvd., Room 713 Arlington, VA 22230-1954 Program Manager: Dr. John Schmisseur	
10. SPONSORING/MONITORING AGENCY REPORT NUMBER			
11. SUPPLEMENTARY NOTES			
12a. DISTRIBUTION AVAILABILITY STATEMENT		12b. DISTRIBUTION CODE	
Approved for public release, distribution unlimited			
13. ABSTRACT (Maximum 200 words)			
This work investigated noise sources and the effects of passive mixing and noise control schemes using vortex generating tabs on noise sources. It is believed that such information is necessary for jet noise modeling and provides guidance for active control of jets for noise mitigation that will follow. The bulk of this work attempts to correlate instantaneous large-amplitude features of the far acoustic field to the dynamic evolution and interaction of large-scale structures within the mixing-layer of ideally expanded, high-speed, high Reynolds number jets. Such information is essential for a better understanding of jet noise sources, and jet aeroacoustic modeling and control.			
14. SUBJECT TERMS		15. NUMBER OF PAGES	
		62	
16. PRICE CODE			
17. SECURITY CLASSIFICATION OF REPORT	18. SECURITY CLASSIFICATION OF THIS PAGE	19. SECURITY CLASSIFICATION OF ABSTRACT	20. LIMITATION OF ABSTRACT
U	U	U	

Mixing and Noise in High Speed Axisymmetric Jets

M. Samimy, J. Hileman, and E. Caraballo
Gas Dynamics and Turbulence Laboratory
Department of Mechanical Engineering
The Ohio State University
Columbus, Ohio 43210

In Collaboration with
S. Narayanan
United Technologies Research Center

Final Technical Report
(GDTL 1-2003)

For
AFOSR Grant F49620-00-1-0023

For the Period of
November 15, 1999 – December 31, 2002

April 2003

Mixing and Noise in High Speed Axisymmetric Jets

M. Samimy¹, J. Hileman², and E. Caraballo²
Gas Dynamics and Turbulence Laboratory
Department of Mechanical Engineering
The Ohio State University
Columbus, Ohio 43210

In Collaboration with
S. Narayanan
United Technologies Research Center

Final Technical Report
(GDTL 1-2003)

For

AFOSR Grant F49620-00-1-0023

For the Period of

November 15, 1999 – December 31, 2002

April 2003

¹ Principal Investigator, Professor of Mechanical Engineering and Director of GDTL

² Graduate Student

ABSTRACT

This work investigated noise sources and the effects of passive mixing and noise control schemes using vortex generating tabs on noise sources. It is believed that such information is necessary for jet noise modeling and provides guidance for active control of jets for noise mitigation that will follow. The bulk of this work attempts to correlate instantaneous large-amplitude features of the far acoustic field to the dynamic evolution and interaction of large-scale structures within the mixing-layer of ideally expanded, high-speed, high Reynolds number jets. Such information is essential for a better understanding of jet noise sources, and jet aeroacoustic modeling and control.

The jet under study had a nozzle exit diameter of 2.54 cm, a Mach number of 1.3, and a Reynolds number of 10^6 . The jet was operated with and without delta tabs to better understand how these noise reduction devices (when used in a chevron configuration) modify the jet and its noise generation mechanisms. Three cases are examined: a baseline (no-tab) jet, a single delta tab jet, and a dual delta tab jet. Power spectra and average acoustic waveform measurements were made for a variety of azimuthal locations; apparent noise origins were determined with an inline microphone array as well as a 3-D microphone array; and temporally resolved flow visualization was used to examine the dynamic flow structure of the jet's mixing-layer. Both of the microphone arrays are unique in they allow for the determination of the origin of individual acoustic 'events' as opposed to obtaining a time-average sound generation region and they were both placed at an angle of 30° relative to the downstream jet axis. The development and application of both of these novel arrays are presented. Conditional sampling of the data from the microphones was used to create characteristic waveforms for the large-amplitude, far-field sound pressure peaks. The frequency content of these phase-averaged waveforms compares well with those of the overall acoustic far-field at 30° . The waveform varied dramatically with downstream location in a manner that is consistent with the long held notion that the dynamic actions of larger scale turbulence structures radiate in a downstream direction.

A vast majority of the large-amplitude sound events from the baseline jet were found to originate between one and two lengths of the jet's potential core and a region that was within a jet radius of the centerline. When tabs were added to the jet the noise generation region moved significantly upstream while also moving away from the tab side of the jet. The acoustic measurements from the inline microphone array were taken simultaneously with real-time flow visualizations to determine the mechanisms that were responsible for the creation of individual far-field acoustic peaks, and these results have identified three noise generation mechanisms for the baseline jet. These include: intense cross-mixing-layer interaction, the tearing of large turbulent structures, and the roll-up of large turbulent structures. While these findings are based on observations, more objective techniques, such as the Proper Orthogonal Decomposition, are currently being used to establish the correlations. The simultaneous data also showed that large structures entrain more ambient air into the jet and the mixing-layer extends farther into the jet core during intense noise production than during periods of relative quiet.

The results from the tabbed jets confirm that the addition of the tabs cause strong streamwise vortices that have a significant effect on both the flow and noise fields of the jet. The addition of tabs causes significant deformation in the cross-stream plane of the mixing-layer, and make the

formation and roll-up of spanwise vortices (due to Kelvin Helmholtz instability) quite regular. Additionally, the noise field becomes azimuthally dependent and the region of noise generation moves dramatically upstream. Based upon these measurements, it appears that the tabs are causing the more regular formation of spanwise vortex roll-ups that lead to noise generation at Strouhal number below 0.6 while the streamwise vortices are responsible for an increase in noise over a range of Strouhal number between 0.8 and 2.5.

The snapshot Proper Orthogonal Decomposition technique was used with LES data obtained for an ideally expanded $M = 1.4$ axisymmetric jet. The reconstruction of the time traces of the velocity inside the jet shear layer showed that 12 POD modes are sufficient to represent the dynamic flow field at several locations, with 8 modes being sufficient farther upstream. The use of vector POD (velocity fluctuation vector) instead of scalar POD (just streamwise velocity fluctuations) did reduce the energy captured in the first few modes and also changed their rank order, but did not substantially alter the reconstructed flow. It was found that in the early jet development region, the first and dominant mode was axisymmetric followed by either another axisymmetric or asymmetric (probably helical) mode, while higher modes in this region and all the modes farther downstream were more complex and three-dimensional. The amount of energy captured by the first POD mode in the cross-stream planes reduces as we approach the end of the potential core but increases farther downstream, suggesting a process of disorganization and breakdown of initially axisymmetric coherent structures in the interaction region (around the end of the jet potential core) and their reorganization into three-dimensional coherent structures farther downstream. Reconstruction of time evolution of modes confirmed the presence of three different types of structures at the cross-stream plane located at $x/D = 3$; an azimuthal vortex, an apparent helical structure, and a three-dimensional structure associated with vortex pairs. However, the structures farther downstream were observed to be more three-dimensional and not amenable to a simple description.

We are currently using the POD with the experimental data to evaluate the effects of tabs on the POD modes and flow structures. We are also using POD as a more objective means of obtaining correlations between dynamics of the large scale structures in the jet and the far field acoustic radiation.

Table of Contents

ABSTRACT.....	2
INTRODUCTION	5
EXPERIMENTAL FACILITY AND TECHNIQUES.....	8
Anechoic Chamber and Jet Facility.....	8
Microphone Array	8
First Generation Design (Dual Element Inline Array).....	8
Second Generation Design (Four Element Inline Array).....	9
Third Generation Design (Eight Element Three-Dimensional Array).....	10
Validation of the Arrays.....	10
Flow Visualization (pulse-burst laser/ultra-fast camera system)	11
Proper Orthogonal Decomposition.....	12
Proper Orthogonal Decomposition Technique.....	12
Flow Simulations.....	12
EXPERIMENTAL RESULTS.....	14
Jet Flow Interrogation.....	14
Average Flow Images (baseline).....	14
Centerline Mach Number (baseline)	14
Average Flow Images (with tabs)	14
Instantaneous Flow Images	15
Acoustic Measurements.....	15
Acoustic Spectra.....	15
Average Acoustic Waveform	16
Noise Source Location	19
Simultaneous Flow/Acoustic Results (baseline Mach 1.3 jet)	21
Simultaneous Flow / Acoustic Data Sets	22
Average “Noisy” and “Relatively Quiet” Images	25
Flow Decomposition with POD	26
POD modes	26
Spatial structure of POD modes	27
Reconstruction of the flow dynamics.....	28
SUMMARY AND CONCLUSIONS	30
ACKNOWLEDGMENTS	34
REFERENCES	35

INTRODUCTION

Since the start of commercial jet travel, aircraft noise has been a nuisance to those living near airports or under flight paths. The exhaust of jet engines is responsible for the majority of noise during the take-off phase of a jet aircraft, and as such has been a topic of research over the past fifty plus years. Significant gains have been made in reducing the noise from jet exhaust simply by following Lighthill's 8th power law (Lighthill, 1952), which shows the sound level from a jet's exhaust is proportional to the eighth power of its exit velocity. By utilizing larger by-pass ratio engines, the effective velocity of the exhaust has been significantly reduced, and the noise levels have dropped. However, additional reductions in noise levels are required and the exhaust velocities of today's engines cannot be lowered much further. As such, different approaches are required for noise reduction.

Most of the previous experimental work in jet noise research has used statistical methods to obtain information on noise sources. These types of techniques have yielded tremendous information regarding the average noise source location, but they have not provided sufficient information about the mechanisms behind noise production. For the most part, the noise emission process has been treated as a 'black box' within the jet mixing-layer, and the relation between the turbulence structures in the jet and noise production has not received enough attention. The reasons for this are many, but the main one has been the lack of experimental methods that can make planar or global, temporally resolved qualitative or quantitative measurements within a high Reynolds number, high speed jet, and then correlate them to the far-field acoustics. The work presented here highlights work that was done to correlate the turbulence structures of a high Reynolds number, high-speed jet to its far-field noise via flow visualizations with simultaneous acoustic measurements.

Turbulent mixing noise is highly directional within the acoustic far-field. The noise emission is most intense at angles close to the downstream jet centerline. The preferred angle has been measured to vary from 25° to 45° with respect to the downstream jet axis (Tam, 1991). An angle of 30° was measured with a peak frequency of approximately 3 kHz, ($St_D = 0.2$) for the Mach 1.3 jet used in this study. The majority of turbulent mixing noise emanates from a region that includes the end of the potential core. This determination has been made by measuring the noise intensity globally over the acoustic near-field (Yu and Dosanjh, 1972, Morrison and McLaughlin, 1979 and Tam, 1991). By using the correlation between velocity fluctuations inside the jet and the far-field acoustic pressure, the noise source region of a Mach number 0.98 jet was determined to be between 5 and 10 jet diameters downstream of the jet exit (Schaffar, 1979). By utilizing various microphone arrays, several research groups have found that the high-frequency noise from high subsonic jets is generated near the nozzle exit, while lower-frequency noise originates further downstream (Fisher et al., 1977, Ahuja et al., 1998 and Simonich et al., 2001).

In studies of low-speed jets and mixing-layers, the noise creation process has been linked to vortex pairing (Kibens, 1980, Colonius et al., 1997, Mitchell et al., 1998). A direct numerical simulation of a low Reynolds number, Mach 0.9 jet showed the far-field noise originated from a region where the computed Lighthill noise sources were both strong and rapidly changing in time (Freund, 2001). Sarohia and Massier (1977) performed experiments with high-speed schlieren motion pictures that were synchronized with near-field pressure measurements. Their study of excited subsonic jets with Mach numbers ranging from 0.1 to 0.9 and Reynolds numbers of up to

10^6 found that large instantaneous pressure pulses were formed whenever two large-scale structures merged; however, the passage of a large structure did not significantly change the near-field pressure signal. These results all indicate a time-varying source is required to generate noise.

The convective velocity of large-scale structures within the jet mixing-layer is a particularly important parameter in this study as it is used to track the location of noise producing events before and after noise is generated. Theoretical equations developed by Bogdanoff (1983) and Papamoschou and Roshko (1988) predict a convective velocity of 206 m/s and a convective Mach number of 0.6 for the Mach 1.3 jet in this study. The actual convective velocity of the large-scale structures has been found to substantially deviate from the theoretical value (Murakami and Papamoschou, 2000). Detailed experimental results of Thurow et al. (2002), which were obtained in the same jet facility as the current work with the use of a MHz rate flow visualization system, indicate that the convective velocity is much higher than the theoretical value. With a large data set of 320 measurements, they found a broad probability density distribution of convective velocities with a mean of 270 m/s. Based on these findings, a convective velocity of 270 m/s is used in the current study.

One effective means of significantly modifying the mixing and acoustic properties of a jet is to introduce strong, streamwise vortices to the flow via small tabs placed at the nozzle exit. Tabs were initially examined because of their ability to eliminate the screech tone from non-ideally expanded supersonic jets (e.g., Ahuja and Brown, 1989 and Samimy et al., 1993). The first research that analyzed how tabs affect the flow field of a round jet was conducted on a low subsonic jet (Bradbury and Khadem, 1975) and this was followed by work on high subsonic and underexpanded supersonic jets (Ahuja and Brown, 1989). Both of these studies used varying numbers of rectangular shaped tabs, and they both agreed that tabs caused: (1) the potential core of the jet to significantly shorten, (2) the loss of the jet's axisymmetric character, and (3) increased entrainment of ambient air into the jet. The flow visualizations of Samimy et al. (1993) showed the dramatic effect of tabs on round jets. Their cross-stream flow images showed that with two tabs, the jet was bifurcated; and additional tabs caused the jet to develop a corresponding number of 'fingers' that completely distorted the jet. These drastic changes in the jet are known to be caused by the presence of strong, counter-rotating streamwise vortices. The presence and properties of these vortices were observed in flow visualizations (Samimy et al., 1993), measured in a Mach 0.3 jet via hot-wire anemometry (Zaman et al., 1994), measured in a very low Reynolds number jet via laser Doppler velocimetry (Reeder and Samimy, 1996), and were quantitatively shown to exist in Mach 1, 1.5, and 2 ideally expanded jets via filtered Rayleigh scattering measurements (Reeder et al., 1996), as well as an underexpanded supersonic jet via 3-D planar Doppler velocimetry measurements (Clancy, 1997). The most effective tabs have a triangular shape, are located at the nozzle exit, and are inclined at a 45° angle to the downstream axis (Zaman et al., 1994). The effectiveness of this configuration, which is referred to as a 'delta tab,' is due to the mechanisms that create the strong, streamwise vortices. The primary source of the streamwise vorticity is the pressure hill that develops upstream of each tab. A secondary source is the shedding of vortex filaments from the sides of the tab (Zaman et al., 1994). When the tabs are inclined in the downstream direction, these two sources augment each other.

Research has also been conducted to determine the effect of delta tabs on the acoustic far-field of heated and unheated Mach 0.9 round jets (Simonich et al., 2001 and Tam and Zaman 2000).

Based on their results, there is not a significant change in the sideline sound levels (perpendicular to the jet nozzle exit) caused by the addition of multiple tabs (up to 8), but there is a shift in the peak frequency. In the downstream direction, which is the direction that is emphasized in this work, adding multiple tabs causes a decrease in the sound level of lower frequencies, but there is a corresponding increase in sound level at higher frequencies. Based on these results, it is apparent that tabs affect the sound generation of subsonic jets or ideally expanded supersonic jets, but the question of *how* such tabs modify the noise generation mechanisms has not been answered.

The examination of turbulent mixing noise in this study focuses on establishing a correlation between the large coherent structures within the jet mixing-layer and the measured noise in the acoustic far-field. This is commonly known as establishing a causality correlation. In an unconventional manner, the acoustic data is examined in the time domain, and is only taken to other domains as necessary when comparison between individual dynamic features and the overall properties of the jet is desired. The jet in this study has a Mach number of 1.3, a nozzle exit diameter, D , of 25.4 mm (1 inch), which is a dimension that will be extensively used in this work as a reference length scale, a Reynolds number based on the jet diameter of 1.08×10^6 , and a potential core length of about 6 jet diameters. The region around the potential core, which is where the majority of the far-field acoustic radiation apparently originates, will be the area of primary interest in this work. To further understand noise generation mechanisms, the effects of tabs (a commonly used noise reduction device) on the noise generation process will also be examined.

EXPERIMENTAL FACILITY AND TECHNIQUES

All of the experiments were conducted in the optically accessed anechoic chamber of the Gas Dynamics and Turbulence Laboratory (GDTL) of The Ohio State University. The facility allows for simultaneous acoustic measurements with real-time flow visualization.

Anechoic Chamber and Jet Facility

The anechoic chamber facility that was used for these experiments is unique in it allows for the measurement of the jet flow with laser diagnostics in a fully anechoic environment. Thus, simultaneous optical measurements of the jet flow and its acoustic field were conducted. The inner dimensions of the chamber, from wedge tip to wedge tip, are 3.12 meters in width and length, and 2.69 meters in height. The chamber was tested for compliance to ANSI Standard S12.3535, and the results from the tests were within the required tolerance over most of the distances along the microphone paths (Kerechanin et al., 2001). The air for the jet was supplied by two four stage compressors; it was filtered, dried, and stored in two cylindrical tanks with a total capacity of 42.5 m^3 at a pressure of 16.5 MPa (1600 ft³ at 2500 psi). A stagnation chamber was used to condition the jet air before exhausting it through a 25.4 mm (1 inch) nozzle with a lip thickness of 2.5 mm (0.1 in) where the inner contour was determined by the method of characteristics for uniform flow at the exit. The actual Mach number of the nozzle was measured as 1.28. Additional details of the anechoic chamber and jet flow facility can be found in Hileman and Samimy (2001) as well as Kerechanin et al. (2001).

Microphone Array

The purpose of this line of research is to relate the *dynamics* of large turbulence structures to the emission of sound; hence a unique approach is required. Conventional methods of noise source localization that rely on analysis of the frequency domain (i.e. cross-spectral measurements) will not work. What is needed is a temporal domain analysis where the origin of *individual* sound events can be determined. Such a sound origin could then be compared to flow measurements of the large structures. Based on this special need, a novel approach was taken in the design of an acoustic array.

First Generation Design (Dual Element Inline Array)

The first generation array design consisted of two microphones that were separated by 5.0D (127 mm) and aligned with the jet centerline. Dynamics of large-scale flow structures are widely believed to create sound that radiates in the preferential downstream direction, which for the current jet was measured as 30° with respect to the downstream jet axis; therefore, the microphone array was placed in this direction. Although this unconventional array location is not optimal for the localization of noise sources, it was considered necessary to accurately capture the sources of the large-amplitude, low-frequency noise traditionally associated with the turbulence mixing generated by large-scale structures. The array was able to locate *individual* sound waves (throughout, a sound wave is any temporal acoustic peak that exceeds a set threshold) by measuring the phase lag between a sound wave reaching the two microphones. Segments of sound data that were 0.35 ms in length (350 data points) were cross-correlated with

equal-length segments from the other microphone signal to determine the time delay between the two microphones recording the event. With this time delay and the microphone positions relative to the jet exit, the origin of the sound wave was determined assuming a constant velocity linear path (simple ray tracing). All of the noise sources were assumed to be distributed along the jet centerline.

The noise source location technique needs to be instantaneous because the source origins are going to be compared to real-time images of coherent structures and their interaction. To do this, one has to relate the time of noise emission to the time the flow image was captured by laser flow visualization, i.e. one needs to measure the time lag between the flow visualization and the emission of the sound wave by the noise source. Equations 7 through 9 of Hileman and Samimy (2001) were used to determine the streamwise location of the noise-emitting region of the jet during the time of laser illumination. These equations have been used throughout this line of research to relate the noise emission time to the laser illumination time.

Unfortunately, the laser will often not be illuminating the flow while the peak sound generation is occurring; thus, one has to take many sets of data to capture a few noise-producing events while they are creating significant sound. This is clear if one considers that the total illumination time of the flow in the acquired movies is limited to 150 μ s (approximately 1.6 convective time scales of D/u_c) while the period of the peak noise at the 30° location (3 kHz) is about 333 μ s. That is, often the flow is illuminated during a period of intermediate noise generation, and not during the most intense noise emission. Ideally, the flow visualization image set would span a time period longer than 333 μ s. The development, associated algorithm and use of this array are summarized in Hileman and Samimy (2001).

Second Generation Design (Four Element Inline Array)

The initial dual microphone array was improved upon by expanding the array to four microphones along a line, which is the second generation microphone array design. The array was comprised of four, 6.35 mm (1/4 inch), 4939 Brüel & Kjaer microphones that were separated by 38.1, 50.8, and 63.5 mm (1.5, 2.0, and 2.5 in.). The use of four microphones provided for six different time delays that lead to six different estimates for the event origin. These six locations were then averaged to determine the average noise source location. Any of the six origins that were located outside the range from -5D to 25D, with respect to the nozzle exit, were not included in the average as they were likely in error.

These separations as well as the physical location of the array relative to the jet nozzle are shown schematically in Figure 1. An aluminum block surrounded by 5 cm thick acoustic foam housed the microphones. Based on the inherent tolerance in the machining of the microphone holding block, the uncertainty in microphone separation was estimated as 0.05 mm (0.002 in.). All exposed surfaces within the chamber were covered in 1.5 cm thick acoustic foam. The sound data were acquired with a National Instruments PC-6110E data acquisition board at a rate of 1 million samples per channel per second. This fast acquisition rate was chosen to maximize the accuracy in measuring the time delay between an acoustic signal peak reaching any two of the microphones.

Typical sound pressure data recorded by the microphones that comprise the inline array are shown in Figure 2. The time origin corresponds to the first laser pulse illuminating the flow. The four microphones recorded peaks of similar shape and magnitude, but these peaks are

shifted in time (i.e. phase shifted). Even at the largest time delay (between the first and last microphones) the overall shape of the sound wave remains substantially unchanged. This manner of determining noise source location is different than those using a cross-spectral method. For that type of technique, which computes an average noise source location and not an instantaneous source, the microphone spacing should not exceed half of the wavelength of the sound that is being located. For the technique used here, any microphone spacing can be used, as long as there is a high correlation between the microphone signals for the event of interest.

The large negative sound pressure peak of Figure 2 recorded around 3.4 ms was cross-correlated for the six different microphone pairs to determine the corresponding time delays and to show how this technique works. Figure 3 shows the 0.35 ms data segments from each microphone that yielded the maximum correlation. Figure 4 shows the same segments shifted by the computed time delays. The time delays between the peaks recorded by microphones 1 and 2, 1 and 3, and 1 and 4 were used to shift the signals of microphones 2, 3, and 4 to overlap with the microphone 1 signal centered on 3.39 ms. Similarly, the time separation between the signals of microphones 2 and 3 and microphones 2 and 4 were used to overlap their signals to that of the microphone 2 signal forming the second group centered on 3.47 ms. Finally, the separation between the peaks for microphones 3 and 4 was used to align the signals of the two microphones centered on 3.60 ms. As seen in the figure, all six time shifts give good visual correlation.

Third Generation Design (Eight Element Three-Dimensional Array)

With an inline array, one has to assume a distribution of noise sources along the jet centerline. To remove this assumption a third generation array was developed that could locate noise sources in three-dimensional space. The 3-D microphone array (the third generation array) relies on the measurement of the phase lag between an *individual* sound wave reaching different microphone pairs in three-dimensional space. The array consists of eight microphones ($\frac{1}{4}$ inch B&K 4135 and 4939 microphones) that are precisely mounted onto a one inch thick aluminum ring. The ring has an inner diameter of 1.52 m (60 in), and an outer diameter of 1.68 m (66 in). Six of the microphones are equally spaced around the periphery of the ring, while the other two microphones are located 19 cm (7.5 in) downstream of the top and bottom microphones. A schematic of the microphone arrangement that shows the distances separating the microphones is shown in Figure 5. The inline microphones determined the downstream location (x-direction) of noise sources, and the azimuthally distributed microphones determined the noise source location in the y and z directions. Hence, all three spatial components of the source vector are determined. Further details of the array, the associated noise source location algorithm, and its calibration can be found in Hileman et al. (2003).

Validation of the Arrays

A Hartmann tube fluidic actuator (HTFA) was used to test the ability of the second generation four element inline array to locate sound sources (Kastner and Samimy, 2002). A Hartmann tube consists of an underexpanded jet directed into a coaxial tube where the open end of the tube is placed within a compression region of the underexpanded jet and the other end of the tube is closed (Hartmann and Trolle, 1927). The high-speed flow of the jet entering and exiting the tube generates a pulsating flow as well as an intense tonal sound. An HTFA is created by placing a cylindrical shield between the nozzle and the tube (Raman et al., 2000). It is also referred to as a powered resonance tube in the literature. This shield covers a large portion of the open area and

creates a pulsating jet. The HTFA used in this validation created a pure acoustic tone with a frequency of 3.66 kHz along with five harmonics. The opening of the HTFA was 4 by 6 mm and the outer diameter of the HTFA was 12.7 mm. The noise emitting region of the HTFA was expected to be within a region close to its exit since this area has been found to be rich in vortical structures (Kastner and Samimy, 2002). The HTFA was placed so the exiting fluid was aligned with the jet centerline and the back surface of the tube was next to the jet nozzle exit. The inline array was then used to determine the origin of all of the sound events that had amplitude in excess of 1.5 times the standard deviation of the signal. This was performed for 0.6 seconds of acoustic data. The predicted downstream locations are given in the probability density distribution of Figure 6. The peak of the distribution coincides with the exit of the actuator and 90% of the distribution is within $\pm 0.5D$ of the actuator exit. Another experiment conducted with a lower pressure HTFA (the frequency content was only slightly different from that listed above) showed similar results. Since this is a distributed source, rather than a point source, the results indicate that the accuracy of this inline microphone array must be better than $\pm 0.5D$. These results as well as the design of the second generation array were described in Hileman et al. (2002a).

Two different noise generators were used to test the ability of the third generation, 3-D microphone array to locate noise sources. The first was a plasma (spark) generated between a pair of wires at varying frequency while the second was an HTFA that was smaller than that used for the validation of the second generation inline array. The sound from the plasma was approximately a point source, in fact a short line source (the stationary arc), while that from the HTFA was distributed over a small area of moving fluid. The 3-D array was able to locate a point noise source (plasma arc) with a primary frequency that varied from 1 to 10 kHz. The plasma arc was then used as a calibration to determine the offset between the center of the 3-D array and the apparent jet centerline. The 3-D array was also able to determine the area of vortical flow from the HTFA regardless of whether it was creating a pure acoustic tone or broadband acoustic radiation. These results are given in Hileman et al. (2003).

Flow Visualization (pulse-burst laser/ultra-fast camera system)

The flow was visualized via scattering of laser light by condensed water particles within the jet mixing-layer. The warm, moist air of the ambient is entrained into the cold, dry jet air that is exiting the nozzle, thus forming the jet's mixing-layer. Upon mixing, the moisture contained in the ambient air condenses into small particles that scatter laser light and mark the majority of the mixing-layer. The laser was an in-house built pulse-burst laser and the scattered light was captured with a camera from Silicon Mountain Design (SMD, now a subsidiary of Dalsa Inc.). Both systems are capable of operating at a MHz rate. The camera was limited to seventeen frames and the flow visualization image sets in this work consist of sixteen images. A variety of inter-pulse timings have been used. Details of this laser/camera system can be found in Thurow et al. (2002).

The laser was located outside of the anechoic chamber and its beam was redirected into the chamber through a 2.5 cm opening. A frame structure, which was covered with acoustic foam and connected to the ceiling of the chamber, held the optics that were used to create the laser sheet that passed through the jet centerline along the streamwise direction. For all experiments, the SMD camera was placed inside of the chamber. The camera could not be placed outside of the anechoic chamber due to limited laser power and poor sensitivity of the camera. Both the

camera stand and the camera were wrapped in acoustic foam to minimize acoustic reflections.

Proper Orthogonal Decomposition

Proper Orthogonal Decomposition Technique

The POD method is a mathematical tool used to decompose a data set, which contains information on all or at least on most scales of a turbulent flow, into a small number of modes that can capture the dynamically significant structures in the flow. It has been used as an objective method to identify coherent structures in turbulent shear flows (Lumley, 1967). The method provides a spatial basis (a set of eigenfunctions) for a modal decomposition of an ensemble of data, obtained from an experiment or computational simulations. These eigenfunctions, or modes, are extracted from the cross-correlation tensor, and can be used as basis functions to represent the flow.

Details of the POD approach have been provided by several investigators (Lumley et al. 1967, Sirovich et al. 1987, Aubry et al. 1988, and Citriniti and George 2000). The method used in the present work is the snapshot method developed by Sirovich (1987). The snapshot method is more suitable to obtain the POD modes in highly spatially resolved data sets, as the classical method is computationally intensive. Details of the current work can be found in Caraballo et al. (2003).

The objective of the present study was to explore the feasibility of using POD with the experimental data that can be obtained using the Planar Doppler Velocimetry (PDV) technique. The standard PDV technique can provide highly spatially resolved instantaneous velocity and detailed statistical data on any given plane, but it cannot provide *time-resolved* data, due to the shortcomings of both current commercial lasers and CCD cameras (Samimy and Wernet 2000). A technique based on pulse burst laser with a repetition rate of up to 1 MHz and an ultra fast CCD camera with similar frame rate is under development (Thurow et al. 2003). Currently, this imaging system is limited to recording 17 consecutive images on the camera for a 150 μ s pulse burst span from the laser. A question therefore was: could this kind of limited data be used with POD technique to provide information on dynamics of coherent structures for their control?

To assess the feasibility of POD application to PDV data, data obtained using large eddy simulations were used (DeBonis and Scott 2002 a&b). LES resolves a large portion of the spatial scales and associated temporal scales in the flows considered. Therefore, LES data has very high spatial resolution, which is in a sense similar to data from PDV, while providing good time resolution (not currently available via PDV). The POD method of choice is the snapshot method.

Flow Simulations

The data used here were obtained from a 3-D large eddy simulation of a high Reynolds number supersonic jet (DeBonis and Scott 2002 a&b). The LES code combines a five-stage, fourth-order Runge-Kutta time discretization with a standard fourth-order central difference spatial discretization. Stability is maintained by removing high wave number dispersive errors with a sixth-order explicit filter. A compressible form of the Smagorinsky model is used to represent the sub-grid scale stresses. The flow was a Mach 1.4 ideally expanded axisymmetric jet issuing from a 2.54 cm diameter nozzle. The computational domain included both the jet flowfield and

the nozzle geometry. This allows for a realistic development of the jet mixing layer, by providing an accurate representation of the flow conditions at the nozzle exit and the initial jet velocity profile. The computational domain extends 20 jet diameters (20D) from the nozzle exit in the streamwise direction and 10D from the centerline in the radial direction. The computational grid was formed by 301 points in the x-direction (streamwise), 129 points in the radial direction, and 36 points in the azimuthal direction. The grid size in the axial and radial directions was determined from a grid study with preliminary axisymmetric solutions. A grid resolution study for the azimuthal direction found only slight differences in time-averaged quantities between the 36 plane solution presented here and a finer 64 plane solution. The time step used in the simulation was 5×10^{-8} s. For the snapshot POD analysis used here, data at an interval of 80 time steps were used (4×10^{-6} s). The data used were for three cross-stream (y-z) planes at 3D, 6D and 9D.

EXPERIMENTAL RESULTS

Jet Flow Interrogation

Average Flow Images (baseline)

Figure 7 shows two average images that cover different downstream distances, which are given at the bottom of the images. The left-hand image is of fifty images of the baseline (no-tab) ideally expanded Mach 1.3 jet covering a downstream range from 2.5 to 8 x/D ; while the right-hand image is of 450 images taken of the same jet using the temporally resolved flow visualization system over a range of 5.5 to 11 x/D . The bright regions are the two sides of the mixing-layer, and the dark region between them is the unmixed core of the jet. As mentioned in the last section, the visualization of the mixing regions is accomplished by scattering of light from a laser sheet by moisture particles within the mixing region. This technique visualizes a major portion of the mixing region, but it does not illuminate the entire mixing-layer. Average cross-sections are shown in Figure 8 for four downstream locations of 3, 5, 7 and 9 x/D . At all of these locations, the mixing-layer forms a round doughnut. Initially, the doughnut is fairly thin with a large dark region at its core (this is the unmixed core of the jet). At larger downstream distances, the doughnut fills in with mixed fluid and by 9 x/D , the interior has nearly been filled with mixed fluid. Farther downstream, the jet cross-section has a uniform intensity.

Centerline Mach Number (baseline)

As stated in the introduction section, a large portion of the noise emitted by a jet has been found to originate around the end of the potential core. The instantaneous, average, and RMS flow visualizations can give an idea of where the end of the potential core is located; however, these results are subjective, as they mark a major portion, but not the entire mixing region. This is due to the nature of the condensation process. For these reasons, the end of the potential core was measured quantitatively with a pitot tube placed on a traversing mechanism. The flow was interrogated from the jet exit to a distance of 11 jet diameters downstream. The pitot pressure was measured with a mercury manometer, and the pressure at the jet exit was assumed to be equal to the ambient pressure because the jet was operating in the ideally expanded regime. As seen in Figure 9, the centerline Mach number starts to decrease between 5 and 6 jet diameters. This marks the end of the potential core. At this point, on average, the mixed ambient/freestream fluid has reached the center of the jet. Lepicovsky et al. (1987) measured the centerline velocity of a Mach number 1.38, Reynolds number 1.6×10^6 jet using a laser velocimeter, and found it started to deviate from a constant value between 5 and 7 D . Other researchers (Yu and Dosanjh, 1972, Thies and Tam, 1996, Seiner, 1992) measured a similar value for the end of the potential core within a Mach 1.5 jet.

Average Flow Images (with tabs)

Average images of the tabbed jet have been compared with those of the baseline, baseline jet. Two images of the one delta tab jet are shown in Figure 10 for a range of downstream locations from 1 to 5 x/D ; the tab location is at the top of the nozzle in the left side and at the bottom of the nozzle in the right side. The tab side of the mixing-layer has been deflected away from the tab, and the opposite mixing-layer is fairly unaffected until the two sides interact downstream of 3

x/D . This marks the end of the unmixed core region. Figure 11 shows two views of the dual-tab jet over a similar range of downstream locations (1 to 5 x/D). The plane passing through the tabs is shown in the left image, while the tab-normal plane is shown in the right image. The tab-normal plane image shows that the mixing-layer is completely bifurcated with two unmixed cores that end between 2 and 3 x/D . The difference in the length of the unmixed core of the tabbed and tab-normal planes is likely due to the difference in the relative intensities of the images.

Images of the cross-stream of the jet were also taken at a downstream location of 3 x/D . The left image of Figure 12 shows the average of 25 images taken of the cross-section of the jet without any tabs. As would be expected, the mixing-layer is round with a uniform thickness. The middle image of 12 shows the average of 250 cross-stream images for the single-tab jet taken at the 3 x/D location. The delta tab, which is located at the top of the nozzle, has dramatically changed the cross-section of the jet as it has been transformed into a ‘crescent’ shape. The strong streamwise vortices that were generated by the tab have contorted the top of the jet’s mixing-layer while the bottom has remained relatively uniform. When a second delta tab is added to the nozzle, as is the case for the right image of Figure 12, a second set of strong streamwise vortices is created, and the cross-section becomes pinched along the vertical axis (parallel to a line connecting the two tabs). This caused the bifurcation of the unmixed core that was observed in Figure 11. Figures 13 and 14 show schematics of tab arrangement and a pair of streamwise vortices generated by a tab.

Instantaneous Flow Images

The average images that were presented previously were obtained from many individual images. These images have appeared in many of our publications, but are not included here for the sake of brevity. Interested readers are directed to the following for instantaneous flow images. A large number of double pulse flow images, as well as instantaneous cross-stream images, of the baseline Mach 1.3 jet were given in Hileman (2000) with a few of these appearing in Hileman and Samimy (2001). Temporally resolved flow images of the baseline Mach 1.3 jet are given shortly while additional image sets can be found in Thurow et al. (2002, 2003). Instantaneous images of the tabbed Mach 1.3 jets (two temporally resolved image sets) can be found in Hileman and Samimy (2003).

Acoustic Measurements

Acoustic Spectra

The acoustic far-field was measured at various angles with respect to the jet axis to determine the peak noise emission direction for the Mach 1.3 nozzle. This was done by placing a series of microphones at 10° increments along a line that was parallel to and 30 D from the jet axis. The spectra for selected angles between 20° and 90° are shown in Figure 15. The orientation with which the angles were measured is also shown in the figure. The spectra were created from one hundred blocks of 32,768 samples of noise data that were taken at a data acquisition rate of 140 kHz. The amplitudes of all of the spectra were adjusted to 60 D by decreasing the sound intensity by 6 dB for every doubling of distance. The frequency peak has maximum amplitude at an observation angle of 30°. This was also the angle where the overall sound pressure level

(OASPL) peaked. The peak frequency at 30° was measured at about 3 kHz. This gives a Strouhal number, St_D , of about 0.2 for a jet diameter of 2.54 cm, and a centerline exit velocity of 375 m/s. The angle of the peak noise emission matches that for a high Reynolds number Mach 1.5 jet (Yu and Dosanjh, 1972) and a low Reynolds number Mach 1.4 jet (Morrison and McLaughlin, 1979). As was discussed in the microphone array section, once the peak noise emission direction was determined, all of the other acoustic measurements were made at that angle. This result was originally published in Hileman and Samimy (2001). These data were taken for 10 seconds of data in blocks of 8,192 points at an acquisition rate of 200 kHz to get the spectra shown in Figure 16. The distances of the microphones were corrected to a distance of 20 feet as recommended by Viswanathan (2002). These results were plotted against the Strouhal number up to a frequency of 90 kHz. The actual peak of the 30° spectra was actually 0.15.

The addition of a single delta tab appears to increase the radiated sound in the 30° downstream direction for frequencies having St_D above 0.1 without a substantial change at lower frequencies, this is regardless of the relative azimuthal tab location (Figure 17). When an additional delta tab is added to the nozzle lip (they are on opposite sides of the nozzle), SPL values below St_D of 0.25 are substantially reduced in both measured directions, while at higher frequencies there is a noise increase (Figure 17). These spectra would need to be scaled to engine size and weighted for human annoyance to determine any actual noise reduction (see Simonich et al. 2001 for details). The largest increase in sound pressure over the baseline jet occurs with the addition of a single-tab at an azimuthal direction opposite the tab, and this increase is observed for St_D between 0.1 and 0.6. This increased sound region possesses a narrow peak at St_D of 0.52.

The aforementioned, high frequency increase in sound energy has a strong azimuthal dependence. The tab-side of the jet has the largest increase over the baseline case between St_D of 1 and 7 with either one or two tabs. The difference in the azimuthal directions is most dramatic in the region shown in the circle marked 'tab-side.' This peak coincides with a stark difference between the two azimuthal directions of a dual-tab jet. Below this peak, the two azimuthal directions of the dual-tab jet deviate by 2 dB for St_D between 0.2 and 0.3, but are otherwise similar in amplitude; however, above a St_D of 1, the two directions deviate considerably. On a non-tab azimuthal direction (regardless of whether one or two tabs were on the jet), there is a fairly uniform decrease in sound intensity with increasing frequency for St_D above 1, but on the tab side of the jet, there is the marked peak which is followed by a uniform decrease for St_D above 2.5.

The addition of tabs caused an increase in high frequency noise (decrease in waveform side lobe widths) at the downstream location of 30° , as will be presented and discussed in the next section. When the 30° microphone was aligned with the tab, the acoustic waveforms had an indentation that matches an increase in the high frequency acoustic spectra. Regardless of the downstream location (similar measurements were taken at downstream locations of 60° and 90°) or number of tabs used, the tab side of the jet has an increase in high frequency acoustic radiation over other azimuthal directions. More of these results are included in Hileman and Samimy (2003).

Average Acoustic Waveform

Traditionally, sound pressure data are examined after they have been Fourier transformed and averaged over extended periods of time to obtain spectral information. In the conversion of the data to the frequency domain, the sound data lose their temporal character, which is needed to

correlate the instantaneous flow structure to large amplitude sound events. In the current work, the sound pressure data are treated in an unconventional manner as they are investigated in the time domain. Short segments of time traces were analyzed to determine the temporal contents of the acoustic data and how various features of the acoustic signature relate to the development of turbulence structures and their interaction in the flow.

A sample time history of the sound pressure for both of the microphones within the array is presented in Figure 18. The time traces show how the sound pressure fluctuates over short periods of time, and with simultaneous flow visualization some of the distinct fluctuations can then be related to the turbulence structures in the jet. An example of such a set of fluctuations is between 1.5 and 2.3 ms of Figure 18 where the sound pressure alternates from negative to positive to negative again with a period of approximately 0.3 ms. Groups of oscillating large amplitude peaks, similar to those between 1.5 and 2.3 ms in Figure 18 were observed in many other acoustic time signatures.

In addition to the expected groups of oscillating, large amplitude, seemingly related, peaks, there were also individual large amplitude peaks. Figure 19 shows an example of such a large amplitude, sound pressure event. This event, marked 'o,' is a positive pressure fluctuation with a magnitude of 95 Pa. This noise event is very similar to the crackle phenomenon observed by Ffowcs Williams et al. (1975) in the Olympus engines used in the Concorde. They observed that the Olympus engine created a series of sharp compressions (positive pressure peaks), crackles, that were followed by gradual expansions. A typical series of compressions as measured by Ffowcs Williams et al. consisted of about 10 peaks, and this could persist up to 0.1 s. The strength of the compressions was about 500 Pa at a distance of 50 m. They used the skewness of the sound data as a measure of crackle. If the skewness was less than 0.3, the jet was not considered to be crackling, while a jet with skewness in excess of 0.4 was crackling distinctly. They attributed the crackling phenomenon to non-linearities at the source, and not to non-linear wave propagation. To confirm whether or not the current jet was crackling, a statistical analysis was performed on the sound pressure data from both of the microphones within the array. A histogram of the sound pressure data from the two microphones within the array was presented in Hileman and Samimy (2001). The distribution appeared to be Gaussian with a computed skewness under 0.1. This is well below the criteria set by Ffowcs Williams et al. Thus, these large amplitude events are not considered to be crackle by the given definition. This is consistent with the work of Ffowcs Williams et al., as they found a similar Mach number jet did not crackle.

In Figure 19, the time range from 1.0 to 2.0 ms for the front microphone has no peaks in excess of 30 Pa, which corresponds to 1.5 times the standard deviation, σ , of the microphone sound data. This is a large period of time without any significant sound events. To give a physical meaning to a 1 ms time period, a large-scale structure traveling at 270 m/s (the convective velocity obtained experimentally for the current jet as determined by Thurow et al., 2003) would convect nearly 12 D over this time period. There are similar periods of relative quiet (defined as having no sound pressure peaks in excess of 1.5σ) in the front microphone time traces of Figure 18 between 2.5 and 3.3 ms and Figure 19 between 2.5 and 3.1 ms, in addition to many other data sets not shown here.

These results are typical of all of the far-field measurements taken at the peak emission microphone location of 30°. There were time signatures that have individual peaks or periodic peaks, and there were significant periods without any large peaks. In some instances, all three

occur over a range of a few milliseconds. These results indicate that there exist various mechanisms within the jet that create individual or repeating large amplitude noise events, and at other times there is no mechanism present that would create intense noise at the 30° location.

All of the sound pressure events with acoustic peaks in excess of 2.0σ were phase-averaged to create a representative waveform for these events. This was performed on the baseline Mach 1.3 jet here and similar work has been performed on the tabbed jets in Hileman and Samimy (2003). One millisecond of data before and after every peak exceeding 2.0σ , where the peaks had been phase-aligned, were ensemble averaged to obtain the phase-average waveforms. This process was performed separately for the positive peaks (910 events) and negative peaks (833 events) to get corresponding phase-averaged waveforms. The analysis was then repeated with a 1.5σ threshold. In this case, 2307 positive and 2259 negative peaks were ensemble averaged from 2.0 seconds of data to get phase-averaged waveforms. The positive phase-averaged waveforms for both threshold levels are shown in Figure 20 along with a Mexican hat wavelet that will be discussed later. All three have been normalized by the standard deviation of the acoustic data. The negative waveforms, not shown here, bare enough similarity to the positive waveforms of Figure 20 that if they were rotated 180° about the origin, the corresponding positive waveform would be created.

The shapes of the waveforms are quite remarkable. They have sharp, distinct peaks with side lobes on both sides of the central peak. The central peak of the 2.0σ threshold waveform has a magnitude of about 2.6, while the side lobes have absolute values of about 0.7 and 0.9. The main peak for the 1.5σ threshold waveforms has a magnitude of 2.2, while the side lobes have equal values of about 0.6. Since the 1.5σ waveform has equal magnitude side lobes, the asymmetry in the side lobes of the 2.0σ waveform must be due in some way to the higher intensity of those sound waves.

The phase-averaged waveform also shares a strong similarity with the Mexican hat wavelet. A wavelet analysis is often used to determine how the frequency of a signal is changing with time. In this type of analysis, a wavelet is convoluted with the signal of interest. To determine what the frequency content is within the signal, the wavelet is stretched or compressed by a multiplier known as the scale. The convolution is then performed with the wavelet for varying time delay, which is referred to as translation. By changing the scale and the translation of the wavelet, the energy contained within various scales (frequencies) can be determined over the duration of the signal. There are an infinite number of wavelets available for study, but a few are commonly used. One of these is the Mexican hat wavelet, which got its name from its similarity to a Mexican sombrero. Figure 20 also includes a Mexican hat wavelet. The Mexican hat wavelet has a slightly broader central peak and side lobes with larger magnitude than that of the 1.5σ phase-averaged waveform. Otherwise, the match of the wavelet and waveform is good. Because of these similarities, the acoustic data from the simultaneous measurements were transformed with the Mexican hat wavelet to determine the time-varying frequency content of the sound data.

The 1.5σ phase-averaged waveform was transformed to the frequency domain and converted to a power spectral density plot. This spectrum is given in Figure 21 along with the conventional spectrum. The frequency content of the spectrum around the peak frequency from the 1.5σ threshold waveform has a remarkable similarity to the conventional spectrum. The strong match of the spectra from the phase-averaged waveforms and the overall far-field radiation shows how well the average waveform is capturing the dominant noise characteristics of the jet at the 30°

observation angle. This has tremendous implications for understanding the correlation between turbulence structures and far-field acoustic, flow/acoustic control, and aeroacoustic modeling. Since the phase-averaged waveform was created by averaging many individual, large-amplitude sound events, and its spectrum accurately recreates the overall spectrum for the jet, it would appear that the large-amplitude sound events are responsible for the generation of the intense low-frequency sound that is observed at shallow angles to the downstream jet axis.

The average waveforms for three downstream locations are compared in Figure 22. These results have been plotted against the convection time scale of a large scale structure (the time was non-dimensionalized by convective velocity and jet diameter). The most notable observation from these data is the stark difference in the waveform shapes for the three directions. The 30° location has a wave shape with distinct side lobes whereas the 60° and 90° locations are dominated by a single narrow peak without any side lobes. The 30° waveform has a 3.2 time scale (0.3 ms) separation between its two negative side lobes and it is 0.6 time scales (0.06 ms) wide at 1.0σ . However, the other two downstream locations do not have large side lobes and are less than 0.1 time scales (0.01 ms) wide at 1.0σ . The differences in the acoustic waveform widths can be directly correlated to the previously given acoustic spectra. The width of the 30° waveform would have a frequency of $1/0.3$ ms, which is 3.3 kHz. This matches the broadband peak of the 30° spectrum ($St_D = 0.15$). The spectra for the 60° and 90° locations do not have any such peak as they are evenly distributed over a broad range of frequencies. This corresponds well to the spectra from the waveforms for the 60° and 90° waveforms, which are also broadband (a single peak in the time domain corresponds to a flat spectrum in the frequency domain).

The time scales of the waveforms correlate well with the structure scales that are known to dominate the production of acoustic radiation in the two extreme directions (30° and 90°). The smaller scales, which have acoustic radiation that dominates at the 90° location, have a shorter time scale than the larger scales that radiate in the 30° direction. These time scales match the widths of the acoustic waveforms quite well. The 30° waveform also bears a strong resemblance to the acoustic field generated by the interaction (leapfrogging) of two ring vortices where the peak sound emission was found to coincide with the two vortices passing through one another (Bridges and Hussain, 1995, Tang and Ko, 1993, Inoue, 2002) as well as the experiments of Kambe (1986) where two vortices were directed toward each other. The 60° waveform has a shape that is quite similar to the 90° waveform. Based on the preceding argument, this would be an indication that the generation of noise at this location is due to smaller scales.

Noise Source Location

Initially, the dual microphone array (first generation) was used to locate noise sources for comparison to double pulse flow images in Hileman and Samimy (2001), but these results were never statistically analyzed. With the use of the four element inline microphone array (second generation), the number of points that were analyzed increased dramatically, and statistics were performed on the noise source location data. The probability density of the apparent noise emission locations (as computed with the second generation array) for all of the sound peaks in excess of 1.5σ has been plotted in Figure 23. Data points that had a standard deviation in excess of $2.0D$ within the locations determined by the six microphone pairs were not included. This left 5584 data points to be plotted in the figure for the 2.5 seconds of data analyzed. The mean of the

noise source locations was 6.7D and the standard deviation was 2.3D. The vast majority (74%) of the noise sources were located in the region between 4 and 9D; and 98% originated between 1 and 12D. The lack of noise origins upstream of the jet exit gives further credibility to the accuracy of this noise localization technique.

The absolute magnitude of each sound peak in excess of 1.5σ has been plotted versus its origin in the form of a two dimensional probability density distribution (Figure 24). This figure was created from the same set of data that was used for Figure 23. The amplitude has again been normalized by the standard deviation of the acoustic data. The contour levels give the percent of noise events within the two-dimensional bins (the bins are 1D wide along the abscissa and 0.25 units in length along the ordinate). Larger amplitude, but less occurring, sound events apparently emanate from farther downstream than the weaker, but more frequently occurring, events. For example, one can see from the figure that events with an amplitude level larger than 2.5σ originated downstream of 3D. The number of all events drops off considerably after 11D.

The three-dimensional microphone array (third generation design) that was described in the experimental arrangement section has been used to locate noise sources within the jet. The origin for every peak with magnitude exceeding 1.5σ was determined for the baseline and tabbed Mach 1.3 jets. This technique finds the apparent source of individual sound waves that have a peak above the set threshold. For each of the three cases, the streamwise, one-dimensional, and the cross-stream (plane normal to the jet centerline), two-dimensional probability density distributions are shown and discussed here. For the single-tab case, the tab was located at the upper lip of the nozzle (0.0 x/D, 0.0 y/D, 0.5 z/D) and in the dual-tab case, the tabs were located on the nozzle exit at 0.0 y/D and ± 0.5 z/D. The amount of data analyzed for each of the three cases differed: 4.3 sec acquired for the baseline jet, 6.4 sec for the single-tab jet, and 6.5 sec for the dual-tab jet. This yielded 10,255, 19,526 and 20,573 acoustic peaks that exceeded 1.5σ , respectively, for the baseline, single and dual-tab jets (as determined by the top, front microphone of the array). The apparent noise origin for each of these peaks was determined with the 3-D microphone array.

The apparent noise source distributions in the downstream direction for the Mach 1.3 jet with and without tabs are presented in the probability density plot of Figure 25. The bins are 1 x/D wide. Differences between the baseline distributions of Figures 23 and 25 are caused by the 10 kHz low-pass frequency filtering that was applied to data taken with the 3-D microphone array that was not applied to the inline microphone array (Hileman et al., 2002b). The addition of tabs significantly shifts the noise generation regions of the jet. This can be quantified by comparing the means for the three distributions, which are 9.0, 3.8 and 4.5 x/D, respectively, for the no, single and dual-tab cases. Without any tabs, eighty percent of the sound sources were located between 6 and 12 x/D. However, with a single-tab, 84% of the sources were located between 1 and 6 x/D and with two tabs, 82% were located between 2 and 7 x/D. These results are in agreement with the measurements of Ahuja et al. (1998). They found the sound origins moved significantly upstream from a range of 4 to 8 x/D for a baseline jet to between 2 and 3 x/D for a jet with two rectangular, pointed tabs (the tabs were mounted normal to the jet centerline). The upstream shift also matches the flow images where the end of the unmixed jet core shifted from a region between 7 and 11 x/D without tabs (Figure 7) to between 2 and 5 x/D with tabs. (Figures 10 and 11). However, these average flow images do not explain the difference between the single- and dual-tab cases. The average images show the unmixed core of the single-tab jet is longer than that of the dual-tab jet. Based on this observation, one would expect the region of

noise generation for the single-tab jet to be downstream of the dual-tab jet. Instead, the opposite is true as the mean location for the single-tab is 0.7 x/D farther upstream of the dual-tab jet's mean location. The difference could be explained by differences in the mechanisms of sound generation between the two cases. The difference could be that the single-tab noise is generated by the interaction of the turbulence structures that are within either side of the mixing layer while the dual tab noise were caused by gross interaction of turbulence structures that span the width of the jet, but are downstream of the end of the unmixed core.

The y and z-components of the noise sources for the three cases are given in the 2-D probability density contour plots of Figures 26-28. Each of the plots covers the same area and the contour colors show the percent of apparent sound origins that came from each 0.05 D by 0.05 D bin. Also shown in the three plots are the relative positions of the nozzle lip line and tabs. The contour for the baseline jet in Figure 26 is circular with a slight offset from the origin. The means for this distribution are 0.2 y/D and 0.0 z/D. The small shift in the y-direction was consistent with all three configurations (all had a mean of 0.2 y/D) and is likely due to the jet centerline being slightly skewed from a line normal to the microphone plane of the 3-D array.

The addition of a single-tab to the jet causes a dramatic shift in the y and z noise source components as shown in Figures 27. The apparent sound origins for the single-tab case have shifted relative to the circular distribution of the baseline jet as they are now centered below the jet centerline (means of 0.2 y/D and -0.3 z/D). The addition of the delta tab has caused the noise origins to move away from the tab. This can be compared to the average cross-stream flow image (shown in upper left corner of figure) that was taken at a position of 3 x/D, which is close to the mean downstream noise source location. The area of noise generation corresponds to the lower, central portion of the mixing-layer where the spanwise roll-ups were regularly interacting with the bottom portion of the mixing-layer (see Hileman and Samimy, 2003). There were not any sound sources in the area where the streamwise vortices are observed, which is the upper right and left hand corners of the crescent shaped mixing-layer. One has to remember when analyzing these results that the acoustic data was low pass filtered at 10 kHz prior to noise source analysis; hence, the noise sources are only for acoustic waves with frequency content less than 10 kHz. The noise source locations were also computed using the bottom front microphone data to identify the large amplitude events (instead of the top, front microphone) and the resulting distribution of noise sources was nearly identical to the single-tab data given in Figures 26-28.

When two tabs are placed on the jet exit, the cross-stream noise source distribution gets elongated along the y-axis as shown in Figure 28. The means for the noise sources in these two directions are 0.2 y/D and 0.1 z/D. The elongation matches the central region of the average flow image (shown in upper left corner of figure) where spanwise roll-ups were growing and interacting on alternating sides of the mixing-layer (see Hileman and Samimy, 2003). Again, the regions where the counter-rotating streamwise vortices are present (the four corners of the nozzle) correspond to regions lacking sound sources.

Simultaneous Flow/Acoustic Results (baseline Mach 1.3 jet)

After the locations for every large-amplitude peak (using a threshold of 1.5σ) within the 2.5 second data set were calculated using the second generation inline microphone array, they were examined to determine which noise generating events would have occurred during the flow visualizations. Any large-amplitude peak that was (1) created during or within a short period of

time either before or after the flow visualizations, (2) had an amplitude over 2.0σ , and (3) had an origin within the field of view, was further analyzed. This increased amplitude was deemed appropriate because the phenomena that cause larger amplitude sound waves should be more apparent. These requirements reduced the number of sound pressure events to be analyzed from several thousand to 22 events with 5 μs between consecutive flow visualization images and 32 events with 10 μs between flow images.

To fully understand what phenomena are creating these large sound pressure peaks, it is also insightful to examine flow visualization movies that coincide with periods where the microphone array was not recording any large-amplitude events, which is referred to as a “relatively quiet period.” A period of relative quiet was defined as one where the array did not record any sound waves in excess of 1.5σ over a length of time of at least 0.6 ms. This time span is approximately 6 convective time scales of D/u_c . A convective time scale is a time period over which a large-scale structure would travel a distance comparable to the structure’s length scale, which is taken to be D here. During such “relatively quiet” movies, a minimal amount of sound reached the microphone array. Practically speaking, the time traces associated with relatively quiet movies have no large-amplitude peaks between 3.2 and 3.8 ms. There were 12 relatively quiet movies with 10 μs spacing, and 18 movies with 5 μs spacing that met this requirement. Due to the space constraints and to the fact that the 10 μs separation movies show more development of the jet, none of the 5 microsecond movies are presented in this report. However, they were examined in great detail and will be used in the average images that will be discussed in the next section.

Simultaneous Flow / Acoustic Data Sets

The presented data sets consist of images that are separated by 10 μs and the simultaneously acquired acoustic time signature. Figures 29 and 30 form a typical, simultaneous data set. The images of Figure 29 can be viewed as a movie of the development of the mixing-layer of the jet. In the flow visualization images of Figure 29 and others to follow, the scattering of laser light via condensed moisture particles created the white, cloud-like areas that mark a major portion of the mixing-layer. The flow is from left to right, and the images are numbered. The last few images have poor quality because the laser power dropped significantly toward the end of the set of laser pulses. The apparent streamwise noise emission location (assumed to be on the jet axis) is marked with a closed square. An open square marks the region of the jet that passed through the noise emission location at the time the sound event was created. This region of the jet was assumed to be traveling with a convective velocity of 270 m/s; hence, the open square is an *estimate* of the location of the noise source in that frame. The proximity of the squares to the top of the image was chosen to prevent clutter within the images and should not be taken to mean the noise originated above the jet. As was mentioned previously, the inline acoustic array cannot resolve the cross-stream location of the noise source and thus the noise origin was assumed to be on the jet centerline. The image where both squares are lined up was taken close to, or at, the time of peak noise production. An acoustic time trace from the front microphone of the array is given in Figure 30. In all of the data shown, the other three microphones recorded phase shifted events similar to that of the front microphone. The time origin on the abscissa corresponds to the first pulse of the laser illuminating the flow.

Based on the flow image sets that captured noise generation, three noise generation mechanisms have been observed. The first is cross-mixing-layer interaction where a large turbulence structure within one side of the mixing-layer interacts with another large structure on the

opposite side of the mixing-layer across the jet core. The second mechanism is the roll-up of large structures within one side of the mixing-layer. The last mechanism involves a large structure being torn apart. Two of these mechanisms, cross-mixing-layer interaction and tearing, were observed with dual laser pulse illumination and were presented in Hileman and Samimy (2001). In this work, examples of all three noise generation mechanisms are given along with two examples of relative quiet.

Cross-mixing-layer interaction within the image set of Figure 29 is the likely cause of the peak that is marked with an 'o' in the acoustic time signature of Figure 30 (the threshold levels of $\pm 2.0\sigma$ are shown in the figure). This peak was created at a downstream location of 7.9D, about 70 μ sec after the first image was taken. The standard deviation for the noise source location was 0.6D. If the source of the sound moved at a convection speed of 270 m/s, it would have been at 7.2D in the first image and at 9.0D in the last as is marked with the open squares. It would appear that the interaction across the two sides of the mixing-layer produced the large peak. This interaction region is between 7 and 10D in image number 8, which was taken about the same time as the maximum sound generation. There were several other data sets that had similar cross-mixing-layer interaction in areas of noise production.

Two other peaks have been marked in Figure 29. The one marked 'A' was created at 8.7D, 1,010 μ sec before the first image was taken. Thus, the region of the jet that passed through the noise production region, 8.7D, at the instant of noise emission would be at 19.4D by the time the first flow image was taken. Similarly, the peak marked 'B' was created at 5.7D, 609 μ sec before the first image. The region of the jet that passed through 5.7D during noise emission would have convected to 12.2D when the first image was taken. In other words, the regions of the jet, which were responsible for creating sound pressure peaks before 'B,' were downstream of the region being imaged in the flow visualizations. Furthermore, those regions of the jet that caused the peaks recorded after 'o' would be upstream of the imaged flow region.

As mentioned, in addition to the data sets that captured apparent large-amplitude sound emission, there were also data sets that captured the jet while the microphone array was recording a period of relative quiet. One such image set is shown in Figure 31. As can be seen in the acoustic time trace of Figure 32, the period of relative quiet is over 1.8 ms long (~ 18 convective time scales), and the few peaks in excess of 1.5σ were all created long before or after the image set in Fig. 31 was taken. The horizontal lines in the relative quiet acoustic time traces show the 1.5σ threshold levels. Hence, there should not be any significant noise generating events present in the top portion of the mixing-layer. In this image set, there is interaction between the two sides of the mixing-layer between 7 and 8D in images 9 to 13, but this interaction appears to be much less intense than that of Figure 29. This subjective interpretation will be validated to some degree in the next section.

The flow visualization image set in Figure 33 shows the roll-up of a large structure within the top half of the mixing-layer that appears to have generated significant noise. The structure is located between 7 and 8D within image 8 (the structure is inside the white circle), and the sound event that apparently originated from the same region is marked in the time signature of Figure 34 with a small 'o.' The apparent origin of the marked peak of Figure 34 was estimated at 6.5D, and it was created about 70 μ s after the first (Figure 33) and 80 μ s before the last images were taken. The standard deviation in the six individual noise source locations was 1.4D. Assuming a convection velocity of 270 m/s, a large structure at 5.8D in the first frame would be at 6.5D

during noise emission; this same structure (assuming a constant convection velocity) would be located at 7.6D in the last image. The sound wave was created approximately when image 8 was taken. By examination of the roll-up process in the flow images, one can see the open square lags the large, developing structure by about one jet diameter. This is expected since the structure is above the jet centerline, and the calculation assumes it to be on the centerline. If the noise origin were 0.5D above the centerline, then the calculated noise emission location would be 0.8D farther downstream. Thus, there is very good agreement between the origin of the marked large peak and the large structure roll-up. The roll-up of large structures was determined to be the mechanism of sound generation in a large number of other image sets.

During the time period when the images in Figure 35 were taken, the jet was in a period of relative quiet that started at 3 ms and lasted until 4.5 ms, as is seen in the time signature of Figure 36. Through analysis of the array acoustic data, it was determined that no noise events in excess of 1.5σ were produced during this movie set. The relatively quiet period, using the aforementioned definition, is 1.6 ms long, during which a large-scale structure convecting at 270 m/s could travel 16.6D. This period of relative quiet is quite remarkable considering the large roll-up of successive large structures within the bottom half of the mixing-layer (in image 13, the structures are centered at 7D and 9D). The structure at 9D in image 13 was created by the mixing-layer first becoming wavy in appearance (frames 4-6 between 7D and 9D), and then rolling up into a large, round structure (frames 8-14 between 8D and 9D). This process is very much like that described by instability wave theory (Tam, 1991, Morrison and McLaughlin, 1979). The upstream structure (at 7D in image 13) forms between 5 and 7D over the course of the movie set by merging of several structures.

There were additional cases, not shown here, of large structure roll-up within the bottom half of the mixing-layer occurring without large-amplitude sound waves reaching the ceiling mounted microphone array. These vortices, which roll-up in either side of the mixing-layer, are not axisymmetric. If a source of noise were located on one side of the jet, then it is unlikely that it would radiate uniformly in all azimuthal directions. In addition, the microphones located on the opposite side of the source relative to the jet centerline would receive, if they receive it at all, acoustic radiation that has been refracted (e.g. Freund and Fleischman, 2002). Thus, the instantaneous azimuthal radiation pattern caused by a sound source that is located on one side of the jet would probably be non-uniform, and such non-uniformity might explain the inability of this acoustic array to detect the roll-up on the other side of the mixing-layer as an apparent noise source. Further work is needed to resolve this issue.

The image set of Figure 37 shows the tearing of a large structure within the top half of the mixing-layer that is the apparent cause of the marked peak in the far-field acoustic signature of Figure 38. This acoustic event has been marked by an 'o'. The apparent origin for the event was at 8.0D, and it was created about 60 μ s after the first and 90 μ s before the last images were taken. Hence, the apparent noise source would have been at a location of 7.4D in the first frame and at 9.2D in the last (constant convective velocity assumption). The tearing event (marked with a circle in frame 3) is occurring over the first four frames of the image set, and is distinguishable by the growing separation between structures that are enclosed in the circle. As was the case for the other two noise generation mechanisms, structure tearing was also prevalent in other noise-capturing data sets.

To relate the large-amplitude far-field acoustic events to the broadband frequency peak, the time varying frequency of the acoustic signal was computed for each of the cases given above by

calculating the energy density over time and frequency using the Mexican hat wavelet transformation. The scales that were computed correspond to frequencies between 1 and 10 kHz. The wavelet results were fairly consistent, and as such will be discussed with a single figure. Based on the energy maps, the large-amplitude peaks (those marked in the previous acoustic time traces) consistently had large energy content between 2 and 4 kHz. The energy density maps for the relative quiet cases had less energy (as compared to the large-amplitude events) within the frequency range between 2 and 4 kHz during the time of relative quiet. Figure 39 shows these two phenomena. It is the energy density distribution for the acoustic time trace of Figure 36. The large-amplitude events (Figure 36) all have corresponding high energy level in the frequency range between 2 and 4 kHz (Figure 39), while the period of relative quiet lacks energy at any frequency. This further supports the argument that these large-amplitude events are in fact the time domain representation of the broadband peak in the frequency domain that occurs between 2 and 4 kHz.

Average “Noisy” and “Relatively Quiet” Images

As previously mentioned, there were a large number of movies taken during noise production as well as periods where the microphone array was not recording any large-amplitude sound events. Thus, it made sense to compare the average state of the jet (in terms of the flow images) during these two conditions. The average images of these opposing conditions as well as the unconditional average image of the jet (average of randomly selected images) were obtained to make the comparison.

The random average image of the jet was created by ensemble averaging the seventh flow image, out of the 17 images, from 77 random flow visualization sets. An average flow image over a similar range of downstream locations was given in Hileman et al. (2002). Frames from each flow visualization set that had captured a noise event in the process of creating a large sound peak in excess of 2.0σ were also ensemble averaged (54 sets in all). Images from each flow visualization image set that had acoustic signatures matching the relative quiet requirements (from the last section, but with a quiet period longer than 0.76 ms, ~ 8 convective time scales) were also ensemble averaged. This set contained 29 images. Prior to averaging, each of the images was normalized so its maximum intensity would be one. This was done to eliminate problems caused by variations in shot-to-shot laser pulse intensity.

Figure 40 shows the intensity of each of the three average images (“noisy,” “relative quiet,” and “random”) at select downstream locations. Upstream of 7D, the three curves have nearly identical centerline intensity. However, downstream of 8D, the “noisy” image has the largest centerline intensity. Since the intensity is directly related to the amount of condensation particles in the jet and these particles are a direct result of large structures entraining ambient fluid into the mixing-layer, there must be more large structures or the large scale structures must be more robust, enabling them to entrain more ambient air into the jet, during the period of time the ‘noisy’ images were taken than during the ‘relative quiet’ images. This is not surprising as cross-mixing-layer interaction and large-scale structure roll-up were considered to be causes of large-amplitude noise production in this work as well as in Hileman and Samimy (2001). Such an observation is impressive considering it was based on an objective sampling of data, and it was not based on a subjective comparison of flow images to noise source locations.

Flow Decomposition with POD

The POD method was applied to the LES data at the cross-stream planes described earlier. The results can be put into three categories: 1) to deal with issues such as the energy content of each mode and the numbers of modes required to reconstruct the flow field, 2) to explore the nature and dynamics of the large-scale structures in a high-speed jet, and 3) to assess the applicability of the POD method with the type of data that can be obtained using PDV (namely, well-resolved data fields in space but resolved over a short time span). Although the LES data contain the full volumetric information (i.e. three velocity components, density and pressure) at every time step, we will limit our discussions to two-dimensional cross-sections and three components of velocity, similar to what will be available experimentally using PDV. Only limited results will be presented here. Detailed results can be found in Caraballo et al. (2003).

POD modes

The LES data at $x/D = 3, 6$, and 9 contained a total of 850 data sets or snapshots (every 80th computational time steps is a snapshot) at each location. Assuming a convective velocity of 300 m/s and a length scale of one nozzle exit diameter (2.54 cm), the convective time scale is 85 μ s, while the time interval at which the snapshots were sampled was 4 μ s (the simulations time step was 0.05 μ s). Therefore, the available total data length was approximately 40 convective time scale for $x/D = 9$ location and almost 100 convective time scale for $x/D = 3$, which contains a statistically significant number of coherent structure passages. Reduced sets of at least 100 snapshots, using 1 out of every 5 to 8 snapshots, distributed over the entire 850 snapshots available, were used to calculate the POD basis at each section. From now on these sets will be referred to as "ordered data set". Statistical convergence in the percentage of energy captured by the modes was observed. Although in these data sets two consecutive snapshots are weakly correlated, each data set spans 40-100 convective time units, over which the flow processes are decorrelated.

The percentage of captured energy (contained in the streamwise velocity fluctuations only) versus the number of POD modes at each cross-stream plane was calculated. The results showed that first POD mode contains 39%, 17%, and 31% of the energy at $x/D = 3, 6$, and 9 , respectively. In order to capture 90% of the energy, the first 11, 16 and 14 modes are required at $x/D = 3, 6$, and 9 , respectively. Interestingly, the percentage of energy captured by a given number of modes decreases from 3D to 6D and then increases at 9D, and this variation is substantial for the first 20 modes or so. We speculate that this trend is a result of the following dynamics. Structures at 3D, in the jet's early development region, are more coherent. At 6D, around the end of the potential core, strong interactions between structures of merging shear layers take place, resulting in the loss of their organization. By 9D, interactions between structures are not as strong and frequent. Therefore, they reorganize and become more coherent. Observations via temporally resolved flow visualizations of a Mach 1.3 ideally expanded, high Reynolds number jet, are consistent with this trend (Thurow et al. 2003). The implications of such processes on the mixing and noise generation process are not yet understood.

When POD was used with the streamwise plane data, the first POD mode captured around 28%, 17%, and 38% of the energy in sections which extend from $x/D = 1-5, 4-8$, and $7-11$, respectively. To recover 90% of the energy, it requires 21, 24 and 20 modes respectively at each section. While the trend of captured energy is consistent with that obtained in the cross-stream

planes, the modes extracted from such a plane do not account for three-dimensional structures and are quite different. Freund and Colonius (2002) have shown that the nature of modes/structures and the convergence of associated eigenvalues are different when one uses volumetric or planar data for reconstruction of the modes.

In what follows, we will focus on the results that will reveal the dynamical significance of each mode and their streamwise evolution. For quantitative comparisons, reconstructed velocity time traces in the shear layer will be assessed to establish the minimum number of modes required to obtain a good representation of dynamically significant flow features and structures.

Spatial structure of POD modes

The characteristics of the POD modes at each cross-stream plane are now analyzed to explore the nature of the dynamically significant structures in the flow. In analyzing the modes, it should be kept in mind that each mode can be thought of as capturing a dominant flow characteristic that may or may not render itself to visualization or other diagnostic techniques. Figures 41-43 show the first six POD modes for the longitudinal velocity fluctuations at three cross-stream planes. For the cross-stream plane at $x/D = 3$, the first two modes are axisymmetric, showing a ring type structure in the mixing layer region. It is well known that in fully expanded jets, ring vortices dominate earlier in the mixing region. Recent real-time flow visualization in a similar Mach number jet show this feature clearly, with smaller scale structures (mostly streamwise vortices) also riding on these large toroidal structures (Thurow et al. 2003). The third mode is asymmetric, evidently associated with the first azimuthal mode ($m = \pm 1$) with energy levels comparable to that for the second mode. Such azimuthal modes are known to be dominant farther downstream (close to the end of the jet potential core). Higher modes have more complex shapes and contain less energy.

At $x/D = 6$, even the first mode has a more complicated shape and is no longer the dominant mode, having comparable energy levels to that of the second mode, which has an asymmetric shape that can be associated with contributions from an $m = \pm 2$ mode. The higher modes have relatively high energy levels and complexity. This location is close to the end of the average potential core, where significant interactions occur among turbulence structures of the merging shear layers. These complex three-dimensional interactions, believed to be responsible for most of the far field noise radiation, are probably responsible for the reduced organization as well.

At the $x/D = 9$ plane, the energy distribution among the modes is similar to that at $x/D = 3$, where the first mode is dominant, although clearly three-dimensional in nature (compared to the axisymmetric structure near $x/D=3$). The modes contain larger regions of positive and negative values while displaying greater spatial homogeneity. This is probably due to the fact that the structures are quite large at this streamwise location and the associated turbulent kinetic energy is more evenly distributed over the cross section. The observed change in the shape of the first POD mode over the three cross-stream planes is similar to available experimental results in low speed jets, which show that the flow structures are more axisymmetric in the developing jet region (e.g. $x/D = 3$), but become more three-dimensional farther downstream.

The POD modes were also calculated using a vector norm, which basically uses velocity vector rather than a single component of velocity (Rowley et al. 2001). Figure 44 shows the first 6 modes for the streamwise velocity fluctuations at $x/D = 3$ calculated with this approach. It can be observed that the shape of the first mode is the same as in Figure 41, but the percentage of

energy recovered has been reduced. Also there is a change in the order of the next three modes, where mode 2 in Figure 41 appears as mode 4 in Figure 44, and modes 3 and 4 in Figure 41 as modes 2 and 3 in Figure 44, respectively. However the modes of the streamwise velocity fluctuations at the other two streamwise locations ($x/D = 6, 9$) didn't show any major changes, except that the percentage of energy captured by each mode was reduced. For all three cross-stream planes, the total energy captured by the same numbers of modes was higher in the scalar approach than in the vector approach. Similar changes were also observed for the other two velocity components. The results are consistent with the findings of Freund & Colonius (2002) of a smaller energy fraction capture by leading order modes for vector approach relative to that from scalar approach

Reconstruction of the flow dynamics

Time coefficients for each POD spatial eigenfunction computed were obtained by projecting the instantaneous velocity field onto the basis functions. For quantitative comparisons, the time traces of the longitudinal component of velocity at the lip line of the jet ($r/D = 0.5$) at $x/D = 3, 6$, and 9 , for 4 and 12 POD modes were computed and compared with the original velocity. The results showed that including only 4 POD modes allows the capture of the general trend of large amplitude velocity fluctuations due to energetic flow structures. However, the magnitude of large excursions from the mean is much lower than that of the original data, as expected due to the neglect of the higher modes. Using the first 8 modes improves the comparison. However, one needs to include in excess of 12 modes in order to closely match the original results. Similar results were observed for the other two velocity components and also for all three velocity components in the streamwise plane. These results suggest that with 12 POD modes, the velocity field can be reasonably well reconstructed, and the large-scale structures in the flow can be identified.

A three-dimensional reconstruction of the velocity field, using the first 12 POD modes was also performed. A total of 425 snapshots of the 850 available were used, taking every other snapshot, with a time step of $8 \mu\text{s}$ between consecutive snapshots. The time coefficients, as mentioned before, were calculated by projecting the instantaneous velocity field, the 425 snapshots, onto the POD basis. Figure 45 compares the original and reconstructed instantaneous streamwise velocity fluctuations at a given time step ($T_s = 116, t = 0.93 \text{ ms}$) for the cross-stream plane located at $x/D = 3$. The overall comparison is good, but finer details of the original results are smeared out in the reconstruction. Similar agreements are observed at other times as well as in other cross-stream locations.

Animation of the streamwise velocity fluctuations were observed for repeated patterns, similar to the method used by Citriniti and George (2000). To help extract the flow dynamics, the cross-stream velocity vectors (the combined radial and azimuthal velocity components) and the gray scale streamwise vorticity contours along with the streamwise velocity animation were used in each cross-stream plane. Although particular sequences, or a "life cycle" as presented by Citriniti and George in a low Reynolds number and low Mach number jet were not observed, there was recurrence of certain structures or events that will be shown and discussed below.

Axisymmetric vortex ring: The first type of structure observed at the cross-stream plane at $x/D = 3$ is an axisymmetric ring that appears repeatedly, dominating the flow field. Figure 46 presents a sequence of 6 frames showing the reconstructed streamwise velocity fluctuations along with the cross-stream velocity vectors and streamwise vorticity contours at $x/D = 3$. The

frames are presented in time steps with consecutive time steps having a real time difference of 8 μ s. This sequence of streamwise velocity fluctuation images clearly captures the passage of an axisymmetric structure through the plane. The streamwise vorticity contours show negligible vorticity level and the vector plots show primarily radial velocities either pointing inward or outward. Such behavior implies a vortex ring type of structure. The ring starts to affect the flow field on this plane at $T_s = 20$ and its effect reaches a maximum around $T_s = 24$. This type of event has been observed before by Citriniti and George and referred to it as a “volcano-like structure.” This type of structure is observed to repeat itself quite often and is clearly related to the first two POD modes ($m = 0$ azimuthal modes) shown in Figure 41.

Helical vortex structure: The second type of structure observed in the reconstructed movies seems to rotate in the azimuthal direction while passing through the $x/D = 3$ plane. Figure 47 shows a set of frames of the reconstructed streamwise velocity fluctuations images, depicting what seems to be a clockwise rotating helical structure. The streamwise vorticity contours along with the cross-stream velocity vectors at the same time steps show two regions of streamwise vorticity - a much higher positive and a lower negative regions. The positive vorticity region rotates along with the cross-plane velocity component, in the same direction as the helical structure. This type of structure is related to the third POD mode ($m = \pm 1$ azimuthal mode) shown in Figure 41. An interesting observation is that helical structures in such flows are known to appear farther downstream. However, these results indicate that they could also be present farther upstream, but with less frequent occurrence and simple visualizations perhaps cannot extract their presence.

Three-dimensional structures: Another type of event observed in the reconstructed movies can be associated with three-dimensional structures. A sequence of images showing the presence of large peaks and valleys associated with large-scale structures in the flow, are shown in Figure 13. Streamwise vorticity contours along with cross-stream velocity vector fields show pairs of counter-rotating vortices entraining fluid into the regions of high streamwise velocity fluctuations. Such structures are prevalent in flow visualization results of a Mach 1.3 ideally expanded axisymmetric jet (Thurow et al. 2003). It should be noted that the streamwise vorticity associated with these counter-rotating vortices are much stronger than those associated with the flow field of Figure 47. In addition to these three types of events at the cross-stream plane located at $x/D = 3$, there are periods in which there is no clear dominance of any one particular type of structure.

Identification of specific structures using similar three-dimensional constructions at the other two cross-stream planes, $x/D = 6$ and $x/D = 9$, is much more difficult, as the structures are more complex. At the $x/D = 6$ plane, more random and three-dimensional behavior of the structures was observed. There was no clear presence of axisymmetric vortex rings, however, vortices of perhaps higher modes ($m = \pm 2, 3$) appear at times. At the $x/D = 9$ plane, the structures are three-dimensional and larger, with slower evolution and more spatial homogeneity of properties over the cross plane.

When the flow was reconstructed using the vector POD modes, similar structures were observed. However, there was some loss of the finer details. This was expected, since the energy of the modes has changed along with a change in the order of the modes, which would cause some differences in the time coefficient for the vector and the scalar cases. In the context of the jet flow, it appears that the scalar approach might be sufficient in capturing the main characteristics of the flow structures. Again, more detailed results can be found in Caraballo et al. (2003).

SUMMARY AND CONCLUSIONS

The focus of this work was on exploring the correlation between turbulence structures and the acoustic far-field of a high Reynolds number, ideally expanded, Mach 1.3 axisymmetric jet. A microphone array was developed that can locate the source of a single instantaneous sound pressure peak. Such an array was necessary to correlate the dynamics of large structures to the jet's acoustic radiation. Using this array simultaneously with a MHz rate flow imaging system, three different jet configurations were analyzed: baseline (no-tab), single tab and dual tab. These configurations were examined to determine the effect streamwise generating tabs were having on the noise generation mechanisms within a high speed, ideally expanded jet. Proper Orthogonal Decomposition analysis was also developed and used to extract information on the nature and dynamics of large scale structures. The POD is currently being used to aid in obtaining correlation between dynamics of large scale structures in the jet and far field acoustic radiation.

By phase-averaging many large-amplitude sound pressure peaks from far-field microphones, an average waveform was created. The average acoustic waveform showed the time scale differences between the acoustic radiation at 30° and 90° , which corresponds well with the turbulence structure scales that are thought to dominate acoustic radiation in these two directions. The 30° waveform possesses the same dominant frequency content as the overall acoustic field, which should have tremendous consequences in modeling the acoustic sources. This 30° waveform also resembles a Mexican hat wavelet and as such, the Mexican hat wavelet transformation was used to analyze the acoustic signals for their frequency content.

The addition of delta tabs clearly changed the azimuthal character of the jet's acoustic radiation at all measured angles. Regardless of the observation angle, the addition of one or two tabs to the jet caused an increase in high frequency acoustic levels on the tab side of the jet relative to the other sides or the baseline case. The increase was observed for St_D between 0.7 and 2 depending on the downstream direction. At downstream angles of 30° and 60° , the side opposite of the tab in a single-tab configuration has increased low frequency noise as compared to the other azimuthal angles or the baseline jet. These observations were also noticed in the average acoustic waveforms, which can be thought of as the time domain representation of the radiated noise. Without the delta tab, the acoustic radiation was azimuthally uniform, but with the addition of either one or two delta tabs, the acoustic radiation became highly directional.

The addition of tabs has clearly introduced strong streamwise vortices to the mixing-layer of the jet. This was deduced from the average cross-stream images. The addition of tabs is also leading to a more regular formation and roll-up of large-scale structures (spanwise vortices) that form on the tab side of the mixing-layer. With two tabs, the structure roll-ups occur on opposing sides of the mixing-layer in a staggered order.

The distribution of noise sources in 3-D space was determined with the third generation, 3-D microphone array. The downstream distribution for the baseline jet was also determined with a relatively simple inline microphone array. The delta tabs dramatically changed the distribution of apparent sound origins. Without any tabs, the sound origin distribution was centered along the jet centerline with a mean downstream location of $8.0 x/D$. When a single-tab is added at the jet exit, the mean of the downstream distribution shifts upstream to $3.8 x/D$ while the cross-stream distribution is deflected away from the tab. A dual-tab jet has a mean noise source distribution downstream location of $4.5 x/D$, and an oval distribution in the cross-stream plane.

The observed azimuthal acoustic directivity could be explained if the tabs were generating counter-rotating vortex pairs that were generating sound at high frequencies and promoting more coherent spanwise turbulence structures (vortices) that were interacting with the streamwise vortices. The various data presented in this work support such a hypothesis. On the tab side of the jet there was a dramatic increase in acoustic radiation for St_D between 0.7 and 2 over any other azimuthal location and this was true for all downstream microphone positions. At a 30° downstream position, where the 3-D microphone array was located, the increase was largest for St_D of 2, which corresponds to a frequency of 30 kHz. Acoustic data was low pass filtered at 10 kHz prior to noise source location processing, thus the noise source location routine would not determine origins for any such sound waves. If the counter-rotating streamwise vortices were generating acoustic radiation in excess of 10 kHz, then there would not be any noise sources (as determined by the 3-D array) from that region. Therefore, it appears the counter-rotating vortices are involved in the creation of acoustic radiation at frequencies above 10 kHz (St_D of 0.7) that is most prevalent on the tab side of the jet.

The tabs also appear to be altering the radiation of sound at lower frequencies which are typically associated with the larger scale turbulence structures. Such analysis is best done at the 30° downstream position where the noise from larger scales dominate. The 3-D microphone array, which was located at this position, determined that over 80% of the noise sources had a downstream location between 1 and 7 x/D for both 1-tab and 2-tab cases. This region corresponds to the area where spanwise vortices were regularly rolling up and interacting with the bottom half of the mixing-layer. This interacting region is on the opposite side of the jet from the counter-rotating streamwise vortices and is the region where the noise sources were observed in the cross-stream noise distribution. A link between structure roll-up, mixing-layer interaction and noise generation was established in Hileman and Samimy (2001 and 2002); hence, one would expect an area of structure roll-up with strong cross mixing-layer interaction to be responsible for the generation of significant sound. At the 30° downstream position, the most intense acoustic radiation is produced opposite the tab of a single-tab configuration at a St_D of 0.2 (3 kHz), which is slightly higher than the peak of the baseline jet (St_D of 0.15). If these roll-ups colliding with the mixing-layer were the cause of the sound production, then one would expect the maximum radiation to be on the same side of the jet as the interactions, which is the case.

A dual-tab jet also has similar properties where the noise generation region corresponds to the area where the spanwise roll-ups are forming in the mixing-layer. The maximum concentration of noise sources is in the region where the spanwise roll-ups are occurring. The cross-stream noise source distribution has a maximum concentration of noise generation near the jet centerline and the cross-stream images show maximum structure activity in this region as well. Further, the non-tab side of the dual-tabbed jet (90° azimuthal separation) has a higher sound pressure at its peak (St_D of 0.25) than does the tab side (0° azimuthal separation). Apparently, the tabs are causing large spanwise roll-ups to occur more frequently and over a shorter space than was observed in a baseline jet. The regular formation of spanwise roll-ups and their interactions are causing a shift in the peak of the frequency spectrum as well as the increased intensity of the peak. The regular formation and interaction of the spanwise roll-ups might also be the cause of the $St_D = 0.52$ peak in the acoustic spectrum for the single-tab jet (0° azimuthal separation) as well as the $St_D = 0.66$ peak in the acoustic spectrum for the dual-tab jet (0° azimuthal separation), but additional work would be needed to conclusively prove it.

It seems that the counter-rotating vortex pairs that are generated by the tabs are generating sound at high frequencies ($St_D \sim 2$, which is high relative to the peak baseline jet noise at a 30° downstream position of $St_D \sim 0.15$) that preferentially radiates in the tab direction. The tabs also seem to regulate the formation of spanwise roll-ups which have a strong influence on the peak jet noise ($St_D \sim 0.2$) at the 30° downstream position in a direction opposite the tabs.

Noise source localization measurements were made with an inline microphone array located at 30° while flow visualization images were simultaneously acquired. The unconventional array location of 30° was chosen to measure the preferential, high intensity, acoustic radiation in that direction. The flow visualization consisted of both dual pulse laser illumination or were temporally resolved from a pulse-burst laser/ultra-fast CCD camera system. Based on the simultaneous flow visualization/acoustic measurements, three apparent noise generating mechanisms were identified within the Mach 1.3 jet. They include cross-mixing-layer interaction, large structure roll-up, and structure tearing. Periods of relative quiet (as recorded by the microphone array) were also observed and discussed.

The average state of the jet during noise emission was compared to that during periods of relative quiet. The average “noisy” image was obtained by ensemble averaging images taken during time periods of significant noise emission (peak amplitude in excess of 2.0σ) while the average “relatively quiet” image was obtained using the ensemble average of the images taken while the microphone array was recording a period of relative quiet, which was defined as having no sound peaks in excess of 1.5σ . Based on this comparison, there are more large and coherent structures in the jet that entrain the ambient air into the jet during noise emission than periods of relative quiet. This further supports the idea that large structure roll-up and cross-mixing-layer interaction generate noise.

The snapshot Proper Orthogonal Decomposition technique was used with LES data obtained for an ideally expanded $M = 1.4$ axisymmetric jet. The snapshots used span 40 to 100 convective time segments. While consecutive snapshots are weakly time correlated, the correlation level drops over a few snapshots and there are sufficient number of structures over which the POD modes and time coefficients are calculated.

The reconstruction of the time traces of the velocity inside the jet shear layer showed that 12 POD modes are sufficient to represent the dynamic flow field at several locations, with 8 modes being sufficient farther upstream. The use of vector POD (velocity fluctuation vector) instead of scalar POD (just streamwise velocity fluctuations) did reduce the energy captured in the first few modes and also changed their rank order, but did not substantially alter the reconstructed flow. It was found that in the early jet development region, the first and dominant mode was axisymmetric followed by either another axisymmetric or asymmetric (probably helical) mode, while higher modes in this region and all the modes farther downstream were more complex and three-dimensional. The amount of energy captured by the first POD mode in the cross-stream planes reduces as we approach the end of the potential core but increases farther downstream, suggesting a process of disorganization/breakdown of initially axisymmetric coherent structures in the interaction region (around the end of the jet potential core) and their reorganization into three-dimensional coherent structures farther downstream. Reconstruction of time evolution of modes confirmed the presence of three different types of structures at the cross-stream plane located at $x/D = 3$; an azimuthal vortex, an apparent helical structure, and a three-dimensional structure associated with vortex pairs. However, the structures farther downstream were

observed to be more three-dimensional and not amenable to a simple description.

We are currently using the POD with the experimental data to evaluate the effects of tabs on the POD modes and flow structures. We are also using POD as a more objective means of obtaining correlations between dynamics of the large scale structures in the jet and the far field acoustic radiation.

ACKNOWLEDGMENTS

The support of this work by the Air Force Office of Scientific Research is very much appreciated. We acknowledge the help of many colleagues at GDTL, including Brian Thurow, Jeff Kastner, and Walter Lempert. The second and third authors would like to thank the Ohio Space Grant Consortium and DAGSI, respectively, for their doctoral fellowships.

REFERENCES

Aubry, N., Holmes, P., Lumley, J. L. and Stone, E., "The Dynamics of Coherent Structures in the Wall Region of a Turbulent Boundary Layer," *Journal of Fluid Mechanics*, Vol. 192, 1988, pp. 115-173.

Ahuja, K.K and Brown, W.H., "Shear Flow Control by Mechanical Tabs," AIAA Paper No. 89-0994, 1989

Ahuja, K.K., Massey, K.C., and D'Agostino, M.S., "A Simple Technique of Locating Noise Sources of a Jet Under Simulated Forward Motion," AIAA Paper 98-2359, June 1998.

Bradbury, L.J.S. and Khadem, A.H., "The Distortion of a Jet by Tabs," *Journal of Fluid Mechanics*, Vol. 70, 1975, pp. 801-813.

Bogdanoff, D.W., "Compressibility Effects in Turbulent Shear Layers," *AIAA Journal*, Vol. 21, No. 6, 1983, pp. 926-927.

Bridges, J., and Hussain, F., "Effects of Nozzle Body on Jet Noise," *Journal of Sound and Vibration*, Vol. 188, No. 3, pp. 407-418, 1995.

Caraballo and Samimy, "Low Dimensional Modeling of Flow for Closed Loop Flow Control," AIAA Paper No. 2003-0059, 2003

Citriniti, J. and George, W., "Reconstruction of the Global Velocity Field in the Axisymmetric Mixing Layer Utilizing the Proper Orthogonal Decomposition," *Journal of Fluid Mechanics*, Vol. 418, 2000, pp. 137-166.

Clancy, P., *Development and Application of Three-Component Planar Doppler Velocimetry for High Speed Flows*. PhD thesis, The Ohio State University, Dept of Mechanical Engineering, 1997.

Colonius, T., Lele, S., and Moin, P., "Sound Generation in a Mixing-layer," *Journal of Fluid Mechanics*, Vol. 330, August 1997, pp. 375-409.

DeBonis, J.R. and Scott, J.N., "A Large-Eddy Simulation of a Turbulent Compressible Round Jet," *AIAA Journal*, vol. 40, no. 7, pp. 1346-1354, July 2002.

DeBonis, J.R. and Scott, J.N., "Study of the Error and Efficiency of Numerical Schemes for Computational Aeroacoustics," *AIAA Journal*, vol. 40, no. 2, pp. 227-234, February 2002.

Ffowcs-Williams, J.E., Simson, J., and Virchis, V.J., "'Crackle': an annoying component of jet noise," *Journal of Fluid Mechanics*, Vol. 71, Part 2, 1975, pp. 251-271.

Fisher, M.J., Harper-Bourne, M., and Glegg, S.A.L., "Jet Engine Source Location: The Polar Correlation Technique," *Journal of Sound and Vibration*, Vol. 51, No. 1, 1977, pp. 23-54.

Freund, J., "Noise sources in a low-Reynolds-number turbulent jet at Mach 0.9," *Journal of Fluid Mechanics*, 2001, vol. 438, pp. 277-305.

Freund, J.B., and Fleischman, T.G., "Ray traces through unsteady jet turbulence," *International Journal of Aeroacoustics*, Vol. 1, No. 1, 2002, pp. 83-96.

Freund, J. B. and Colonius, T., "POD Analysis of Sound Generation by a Turbulent Jet," AIAA Paper 2002-0072, January 2002

Hartmann, J. and Trolle, B., "A New Acoustic Generator. The Air-Jet Generator," *Journal of Scientific Instruments*, Vol. 4, pp. 101-111, 1927.

Hileman, J., *A study of noise generating large turbulent structures within a Mach 1.3 Axisymmetric jet*, MS Thesis, The Ohio State University, Dept of Mechanical Engineering, 2000.

Hileman, J. and Samimy, M., "Turbulence Structures and the Acoustic Far-Field of a Mach 1.3 Jet," *AIAA Journal*, Vol. 39, No. 9, 2001, pp. 1716-1727.

Hileman, J., Thurow, B. and Samimy, M., "Exploring Noise Sources using Simultaneous Acoustic Measurements and Real-Time Flow Visualizations in Jets," *AIAA Journal*, Vol. 40, No. 12, 2002, pp. 2382-2392.

Hileman, J., Thurow, B. and Samimy, M., "Development and Evaluation of a 3-D Microphone Array to Locate Individual Acoustic Sources in a High-Speed Jet," submitted to *Journal of Sound and Vibration* in October 2002.

Hileman, J. and Samimy, M., "Effects of Vortex Generating Tabs on Noise Sources in an Ideally Expanded Mach 1.3 Jet," will appear in *International Journal of Aeroacoustics*, 2003.

Inoue, O., "Sound generation by the leapfrogging between two coaxial vortex rings," *Physics of Fluids*, Vol. 14, No. 9, pp. 3361-3364, 2002.

Kambe, T., "Acoustic emissions by vortex motions," *Journal of Fluid Mechanics*, Vol. 173, 1986, pp. 643-666.

Kastner, J. and Samimy, M., "Development and Characterization of Hartmann Tube Based Fluidic Actuators for High Speed Flow Control," *AIAA Journal*, Vol. 40, No. 10, Oct. 2002 (Tentative).

Kerechanin C.W., Samimy, M., and Kim, J.-H., "Effects of Nozzle Trailing Edges on Acoustic Field of Supersonic Rectangular Jet," *AIAA Journal*, Vol. 39, No. 6, 2001, pp. 1065-1070.

Kibens, V., "Discrete Noise Spectrum Generated by an Acoustically Excited Jet," *AIAA Journal*, Vol. 18, April 1980, pp. 434-441.

Lepicovsky, J., Ahuja, K.K., Brown, W.H., and Burrin, R.H., "Coherent Large-Scale Structures in High Reynolds Number Supersonic Jets," *AIAA J.*, Vol. 25, No. 11, 1987, pp. 1419-1425.

Lighthill, M.J., On Sound Generated Aerodynamically: I. General Theory. *Proc. Royal Soc. London*, Ser. A., Vol. 211, pp. 564-581, 1952.

Lumley, J., "The Structure of Inhomogeneous Turbulent Flows," *Atmospheric Turbulence and Wave Propagation*, Nauka, Moscow, 1967, pp. 166-176.

Mitchell, B., Lele, S., and Moin, P., "Direct Computation of the Sound Generated by Vortex Pairing in an Axisymmetric Jet," *Journal of Fluid Mechanics*, Vol. 383, October 1998, pp. 113-142.

Morrison, G.L., and McLaughlin, D.K., "Noise Generation by Instabilities in Low Reynolds Number Supersonic Jets," *Journal of Sound and Vibration*, Vol. 65, Issue 2, 1979, pp. 177-191.

Murakami, E. and Papamoschou, D., "Eddy Convection in Coaxial Supersonic Jets," *AIAA Journal*, Vol. 38, No. 4, 2000, pp. 628-635.

Papamoschou, D. and Roshko, A., "The Compressible Turbulent Mixing-layer: An Experimental Study," *Journal of Fluid Mechanics*, Vol. 197, 1988, pp. 453-477.

Raman, G., Kibens, V., Cain, A., and Lepicovsky, J., "Advanced Actuator Concepts for Active Aeroacoustic Control," *AIAA Paper 2000-1930*, June, 2000.

Reeder, M.F. and Samimy, M., "The evolution of a jet with vortex-generating tabs: real-time visualization and quantitative measurements," *Journal of Fluid Mechanics*, Vol. 311, 1996, pp. 73-118.

Reeder, M.F., Samimy, M., and Elliot, G., "Investigation of the Effect of Tabs on Supersonic Jets Using Advanced Diagnostics," *Journal of Propulsion and Power*, Vol. 12, No. 4, 1996, pp. 742-751.

Rowley, C. W., Colonius, T. and Murray, R., "Dynamical Models for Control of Cavity Oscillations," *AIAA Paper 2001-2126*, May 2001.

Samimy, M., Zaman, K.B.M.Q., and Reeder, M., "Effect of Tabs on the Flow and Noise Field of an Axisymmetric Jet," *AIAA Journal*, Vol. 31, No. 4, 1993, pp. 609-619.

Samimy, M and Wernet, M. P., "Review of Planar Multiple-Component Velocimetry in High-Speed Flows," *AIAA Journal*, Vol. 38, No. 2, 2000, pp. 553-574.

Sarohia, V., and Massier, P.F., "Experimental Results of Large-scale Structures in Jet Flows and Their Relation to Jet Noise Production," *AIAA Paper 77-1350*, October 1977.

Schaffar, M., "Direct Measurements of the Correlation Between Axial in-jet Velocity Fluctuations and Far-field Noise near the Axis of a Cold Jet," *Journal of Sound and Vibration*, Vol. 64, No. 1, 1979, pp. 73-83.

Seiner, J.M., "Fluid Dynamics and Noise Emission Associated with Supersonic Jets," *Studies in Turbulence*, edited by T.B. Gatski, S. Sarkar, and G. Speziale, Springer-Verlag, New York, 1992, pp. 297-323.

Simonich, J., Narayanan, S., Barber, T.J., and Nishimura, M., "Aeroacoustic Characterization, Noise Reduction, and Dimensional Scaling Effects of High Subsonic Jets", *AIAA Journal*, Vol. 39, No. 11, 2001, pp. 2062-2069.

Sirovich, L., "Turbulence and the Dynamics of Coherent Structures," Part I,II,III: Coherent Structures," *Quarterly of Applied Math.* Vol. XLV, No. 3, 1987, pp. 561-590.

Tam, C.K.W., "Jet Noise Generated by Large-Scale Coherent Motion." *Aeroacoustics of Flight Vehicles: Theory and Practice*. Vol. 1, edited by H.H. Hubbard, 1991, pp. 311-390.

Tam, C.K.W., and Zaman, K.B.M., "Subsonic Jet Noise from Nonaxisymmetric and Tabbed Nozzles," *AIAA Journal*, Vol. 38, No. 4, 2000, pp. 592-599.

Tang, S.K., and Ko, N.W.M., "A Study on the Noise Generation Mechanism in a Circular Air Jet," *Journal of Fluids Engineering*, Vol. 115, No. 3, pp. 425-435, 1993.

Thies, A.T., and Tam, C.K.W., "Computation of Turbulent Axisymmetric and Non-axisymmetric Jet Flows Using the $\kappa-\epsilon$ Model," *AIAA J.*, Vol. 34, No. 2, 1996, pp. 309-316.

Thurow, B., Hileman, J., Samimy, M. and Lempert, W., B., "A technique for real-time visualization of flow structure in high-speed flows," *Physics of Fluids*, Vol. 14, No. 10, pp. 3449-3452, 2002.

Thurow, B., Samimy, M. and Lempert, W., "Compressibility Effects on Turbulence Structures of Axisymmetric Mixing-layers," accepted to *Physics of Fluids*, 2003.

Viswanathan, K., "Analysis of the Two Similarity Components of Turbulent Mixing Noise," *AIAA J.*, Vol. 40, No. 9, September, 2002.

Yu, J.C., and Dosanjh, D.S., "Noise Field of a Supersonic Mach 1.5 Cold Model Jet," *Journal of the Acoustical Society of America*, Vol. 51, No. 5, Pt. 1, 1972, pp. 1400-1410.

Zaman, K.B.M.Q., Reeder, M.F., Samimy, M., "Control of an Axisymmetric Jet Using Vortex Generators," *Physics of Fluids*, Vol. 6, No. 2, 1994, pp. 778-793.

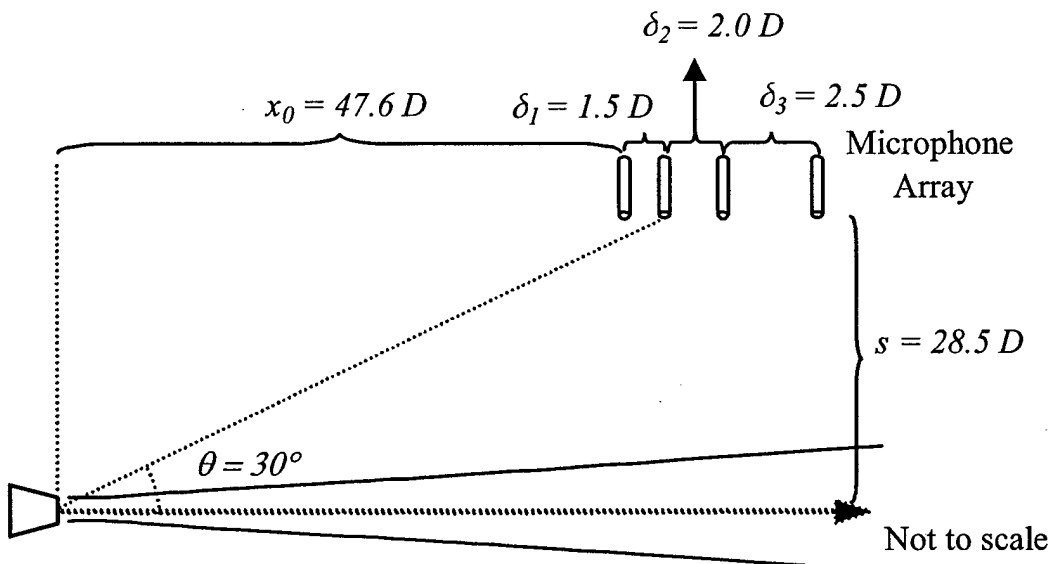


Figure 1: Schematic of the inline microphone array used to determine noise source location.

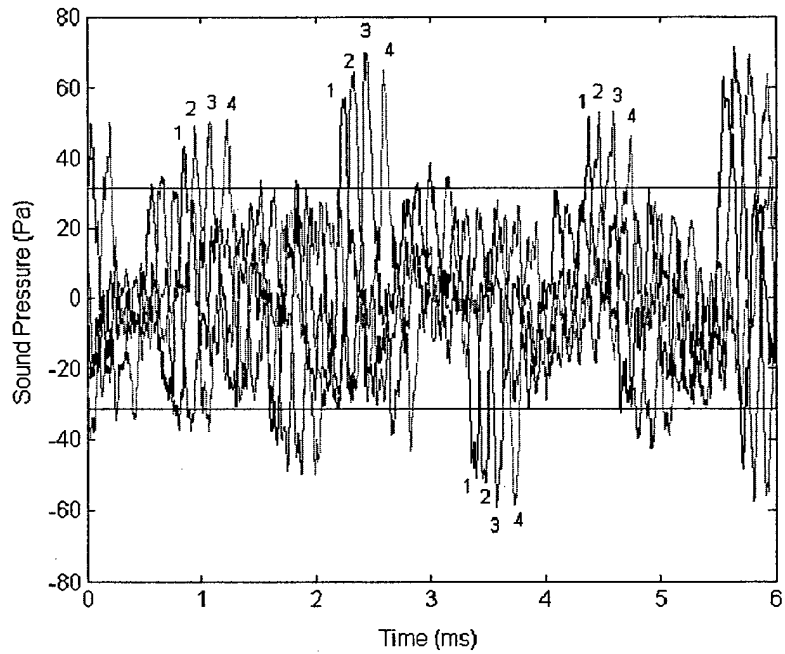


Figure 2: Typical data recorded by the four microphones of the inline array. Time is relative to the first laser pulse illuminating the flow. The numbers correspond to each of the individual microphone signals.

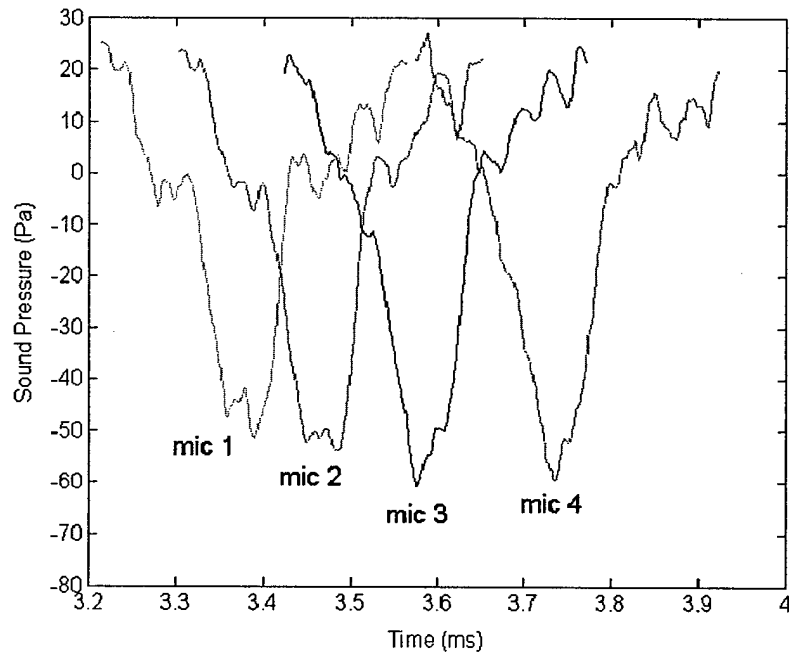


Figure 3: The time segments for each of the four microphones of the inline array that were used to determine the origin for a large-amplitude peak. This is a portion of the time signature in Figure 2.

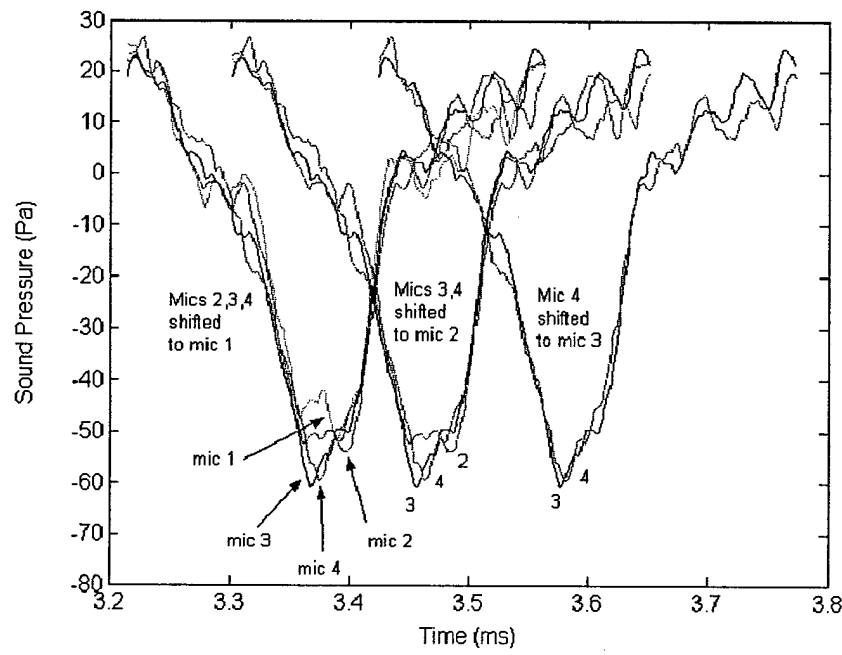


Figure 4: The time segments of Figure 3 shifted by the computed maximum correlation times (time separations).

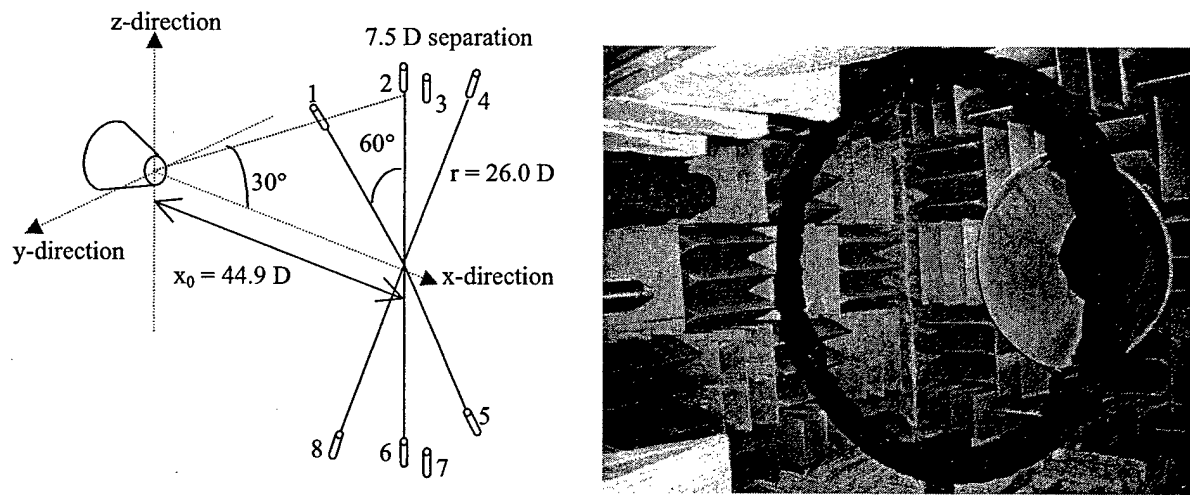


Figure 5: Schematic and photograph of the 3D microphone array that is used to locate noise sources in space.

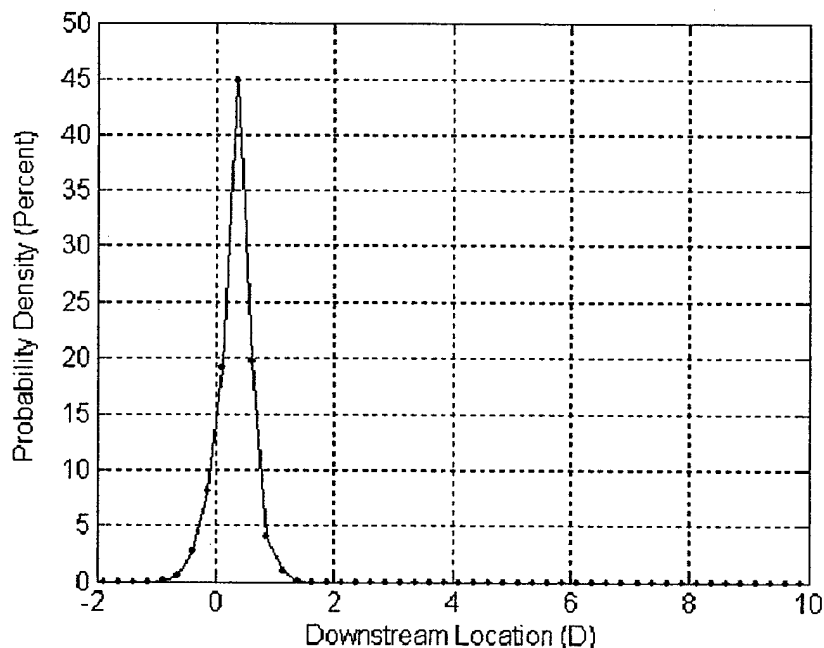


Figure 6: Probability density distribution of apparent noise source locations for the HTFA used to validate the inline array. The abscissa is relative to the rear of the HTFA, which coincides with the jet exit.

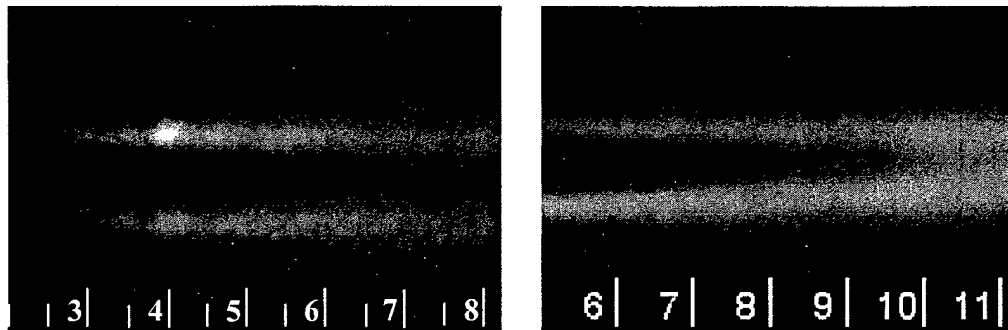


Figure 7: Average streamwise image of the baseline (no-tab) jet.

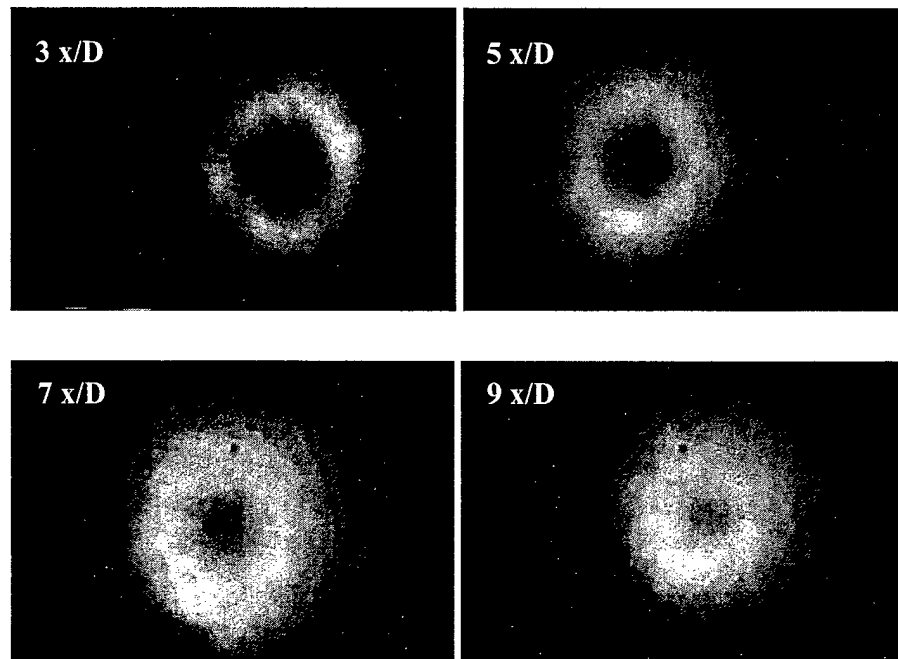


Figure 8: Average Jet Cross Section (images not to scale with one another)

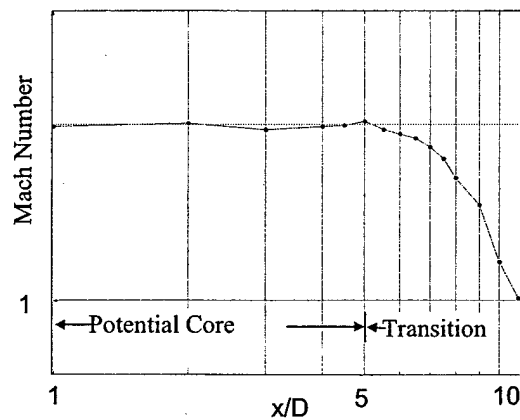


Figure 9: Centerline Mach number versus streamwise distance.

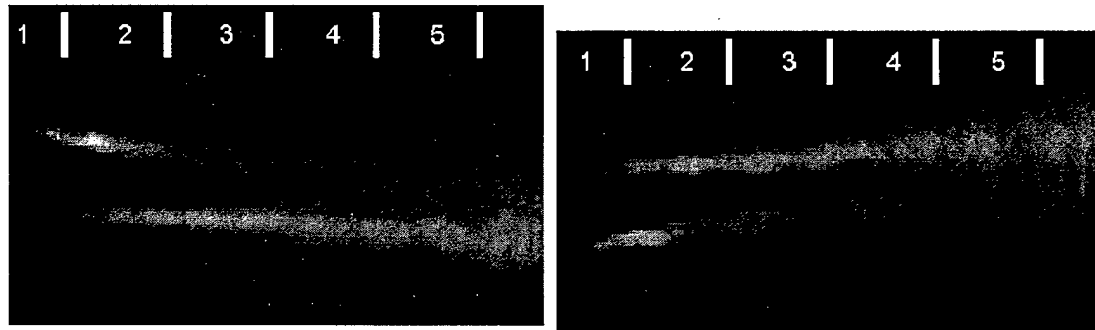


Figure 10: Average of 250 streamwise images for a one- tab jet. The tab was on the top lip of the nozzle for the left image and at the bottom lip of the nozzle for the right image. Downstream distances are marked along the top of the image in x/D .

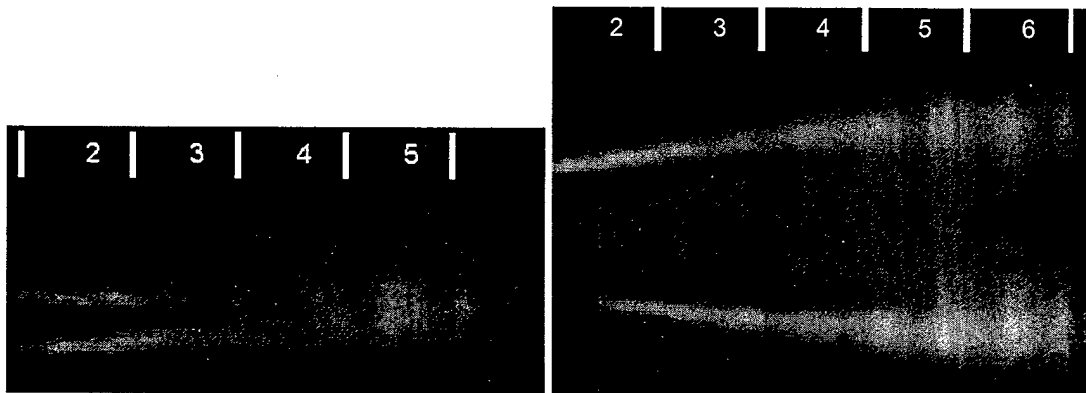


Figure 11: Average of 250 streamwise images of a dual-tab jet. The illuminating and tab planes coincide in the left image and are normal in the right image.

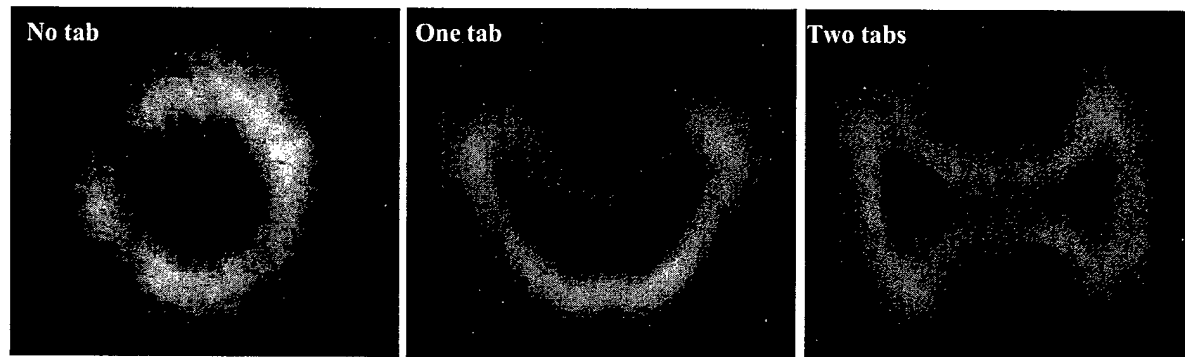


Figure 12: Average cross-stream images taken at a downstream distance of 3 D. The left image is for the baseline jet. The middle image is a single-tab jet where the tab was located at the top of the nozzle. The right image is a dual-tab jet where the tabs were at the top and bottom of the nozzle.

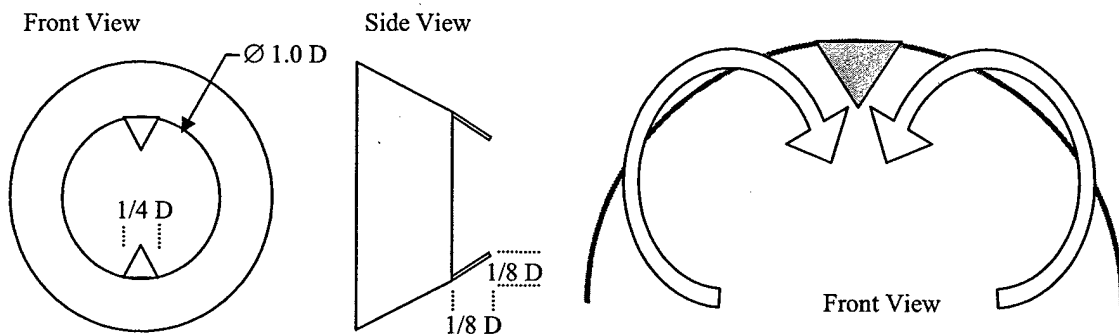


Figure 13: Schematic of two delta tabs mounted on a nozzle. The dimensions used are shown in jet diameter.

Figure 14: Direction of the streamwise vortices that are induced by a single delta tab. View is from downstream of the tab, and the upper half of the nozzle of Figure 13 is shown.

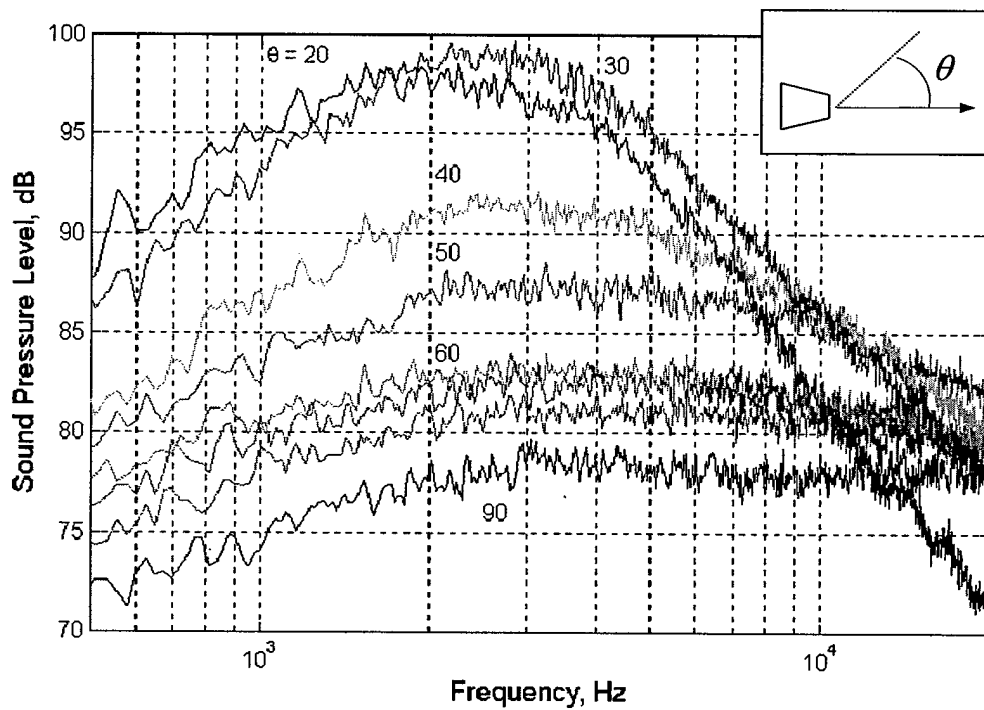


Figure 15: Variation in the far-field acoustic spectra with changing observation angle, θ .

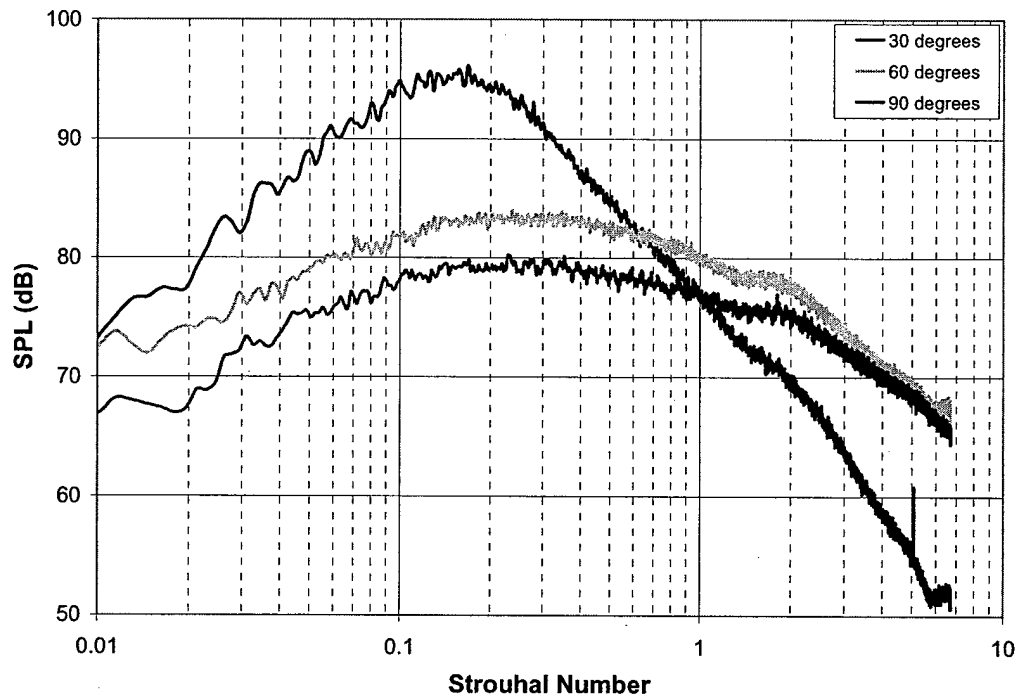


Figure 16: Variation in the far-field acoustic spectra with changing observation angle, θ .

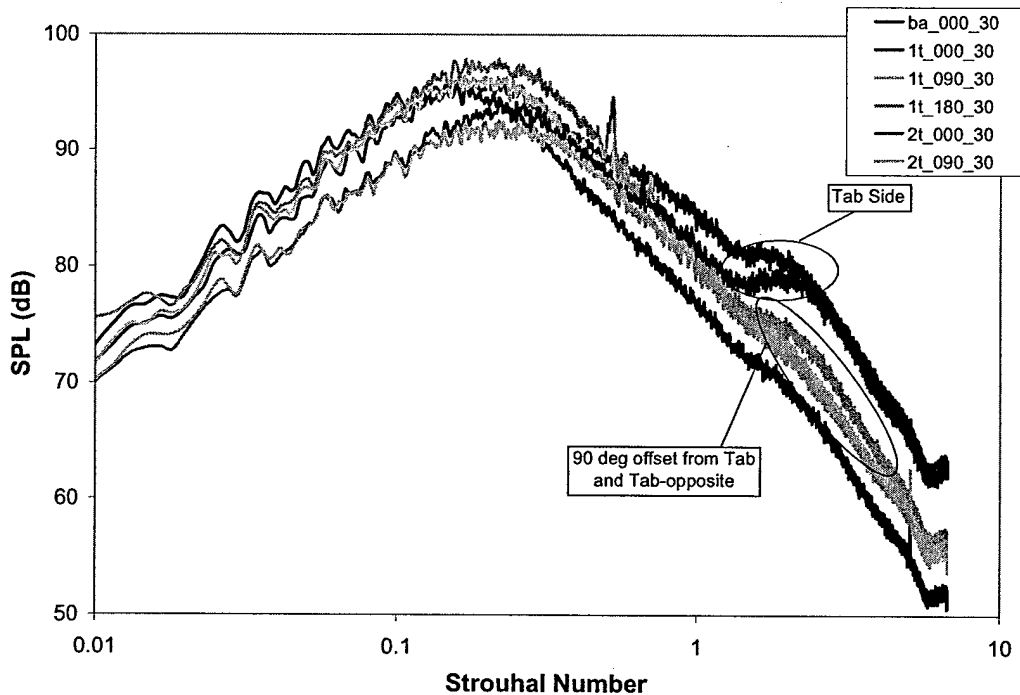


Figure 17: Comparison of the power spectra for the baseline, single-tab and dual-tab cases for the 30 degree downstream location.

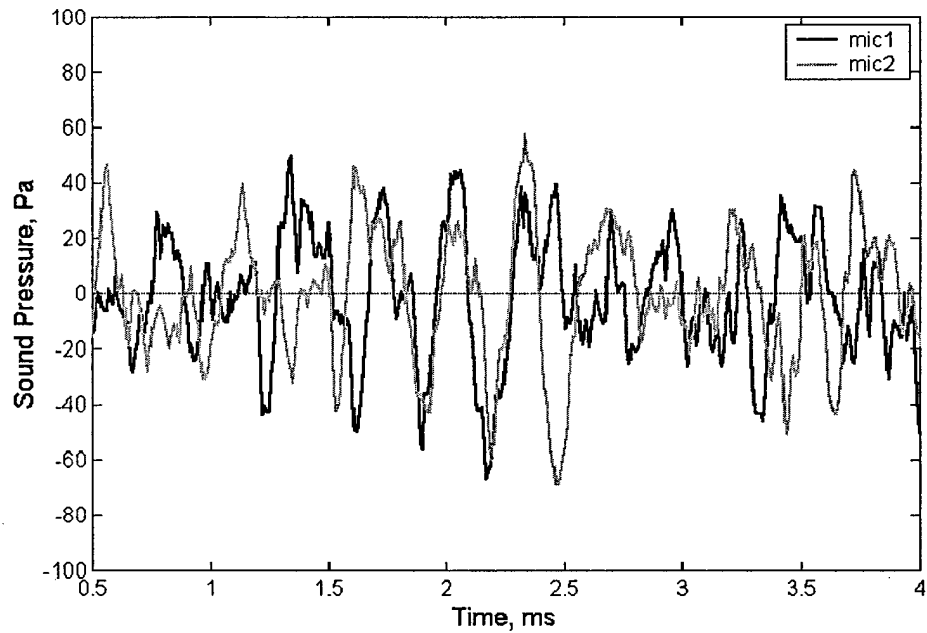


Figure 18: Time trace of the dual element microphone array data showing a series of oscillatory sound pressure peaks.

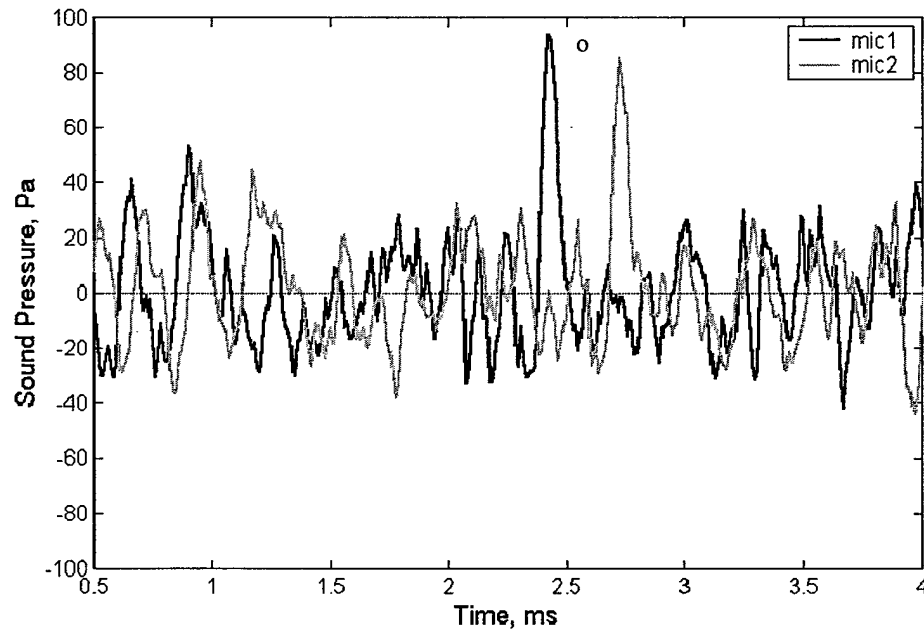


Figure 19: Time trace of the dual element microphone array data showing a single peak and relative quiet periods.

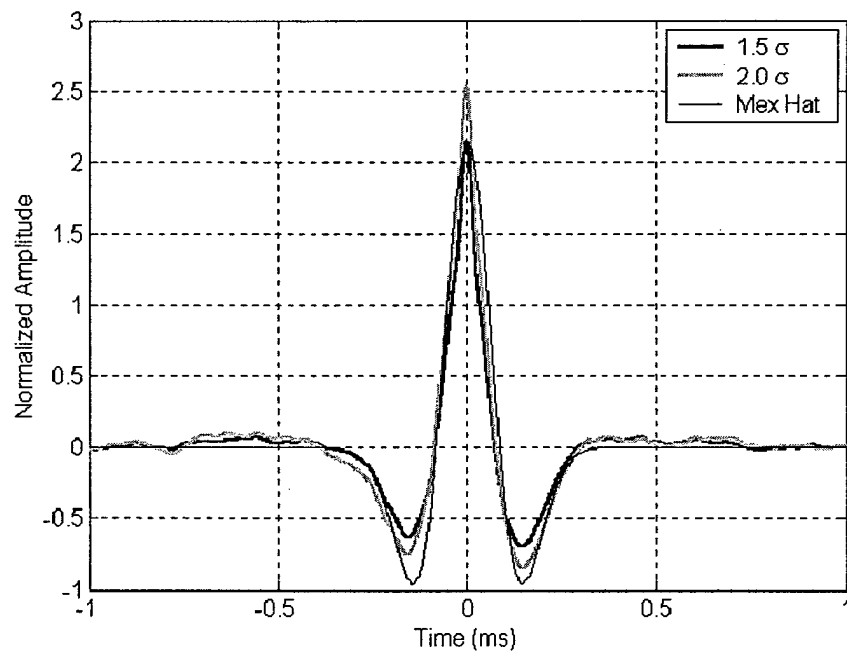


Figure 20: Phase-averaged, positive, large-amplitude, sound pressure waveforms for all of the time trace segments with a peak amplitude larger than 1.5σ and 2.0σ along with a Mexican hat wavelet. Amplitude is normalized by the standard deviation.

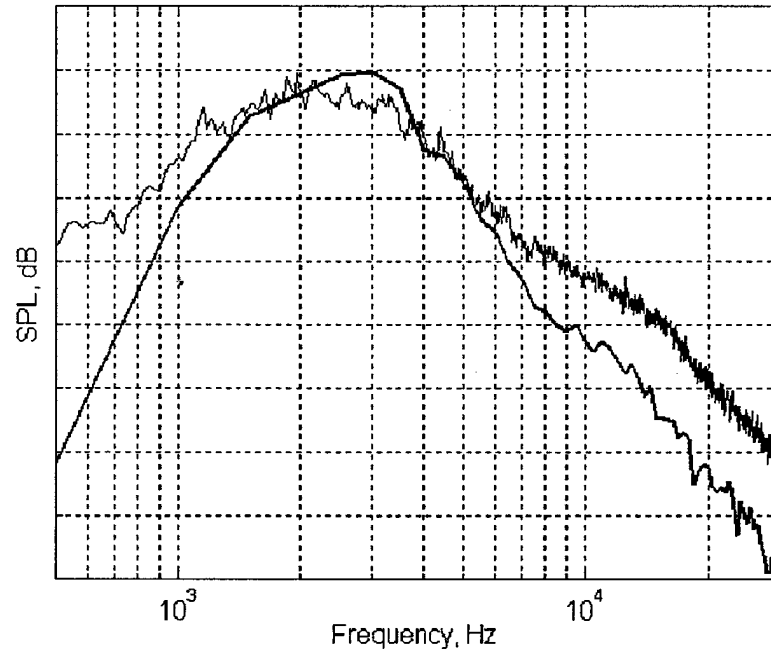


Figure 21: Overall spectrum and the spectrum for the 1.5σ average waveform.

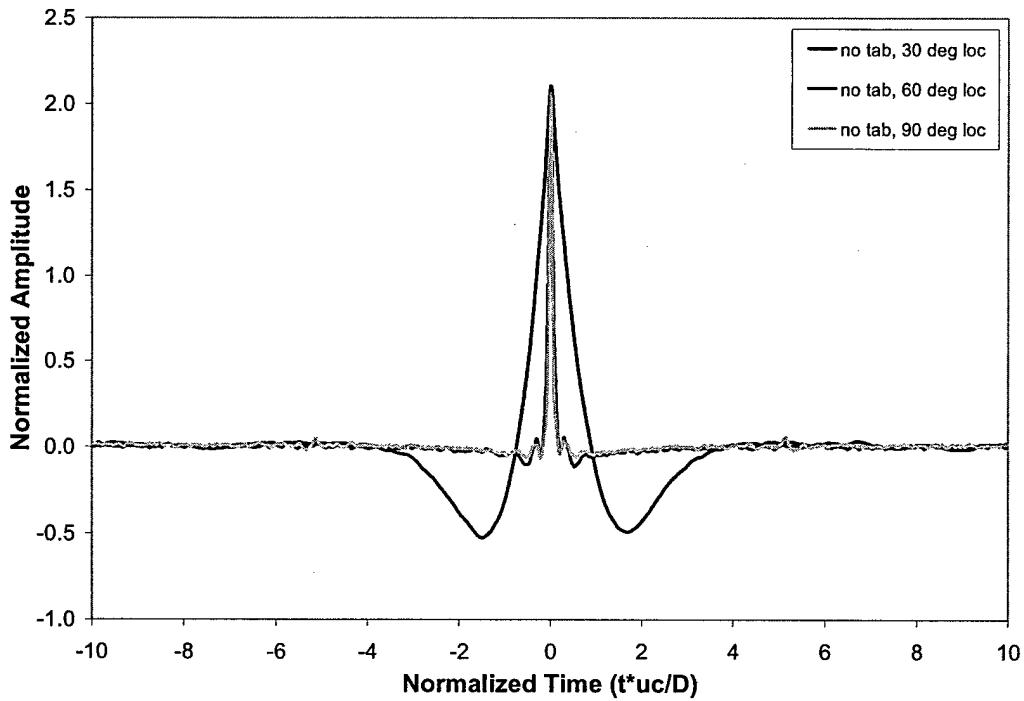


Figure 22: Comparison of the average acoustic waveform for the three different downstream locations (30, 60 and 90°) for the baseline, Mach 1.3 jet.

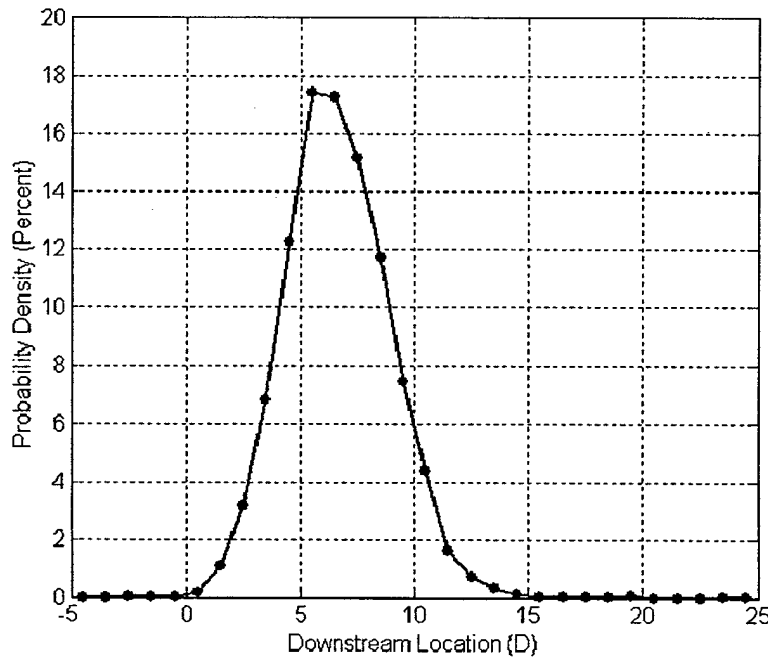


Figure 23: Probability density of the apparent large-amplitude sound event sources (peak amplitude larger than 1.5σ). The dots denote calculated data points that are spaced at 1D and the solid line is a curve fit.

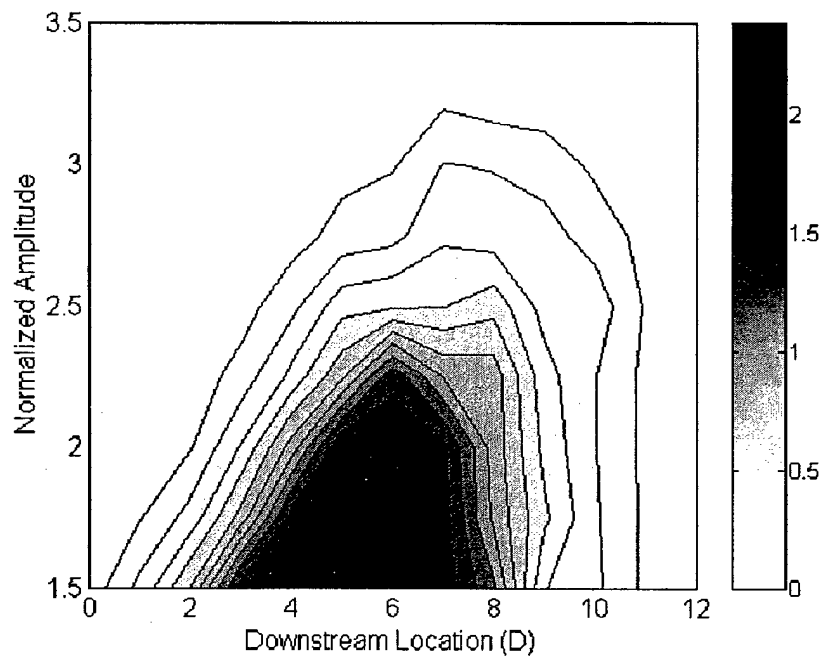


Figure 24: Two-dimensional probability density distribution showing the downstream locations for sound events of varying amplitude.

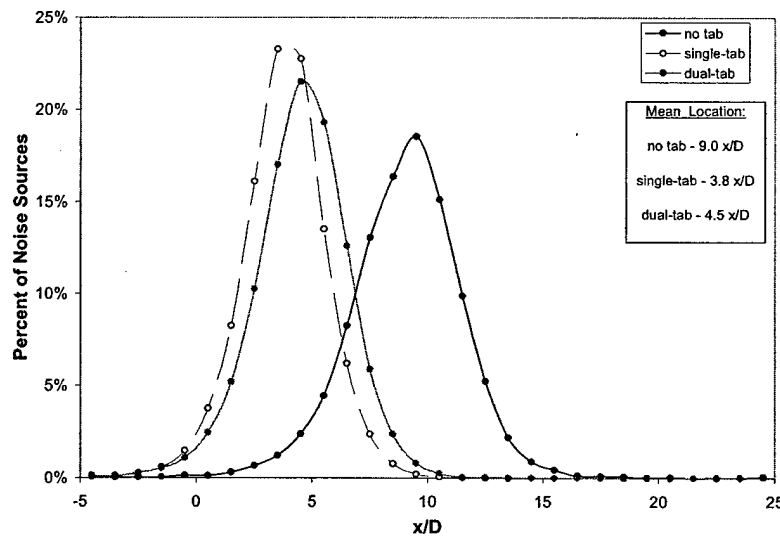


Figure 25: Comparison of the downstream noise source location for the baseline, single-tab, and dual-tab Mach 1.3 jets.

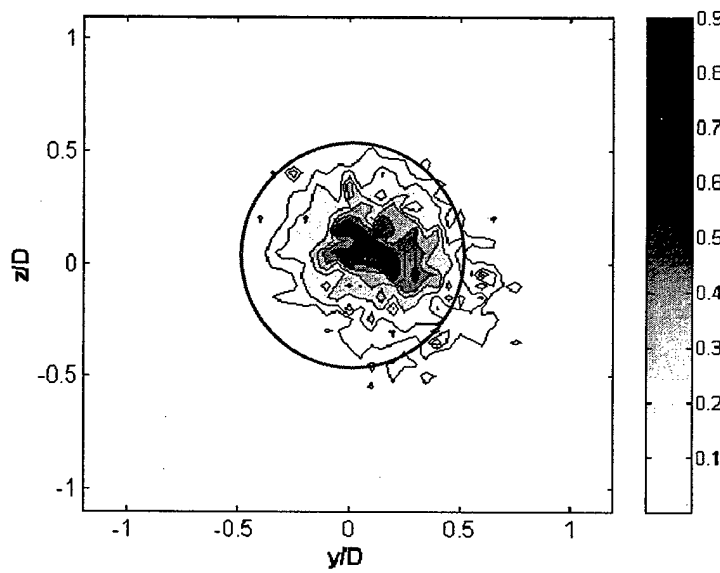


Figure 26: 2-D probability density distribution of apparent noise sources in the cross-stream plane for the baseline jet.

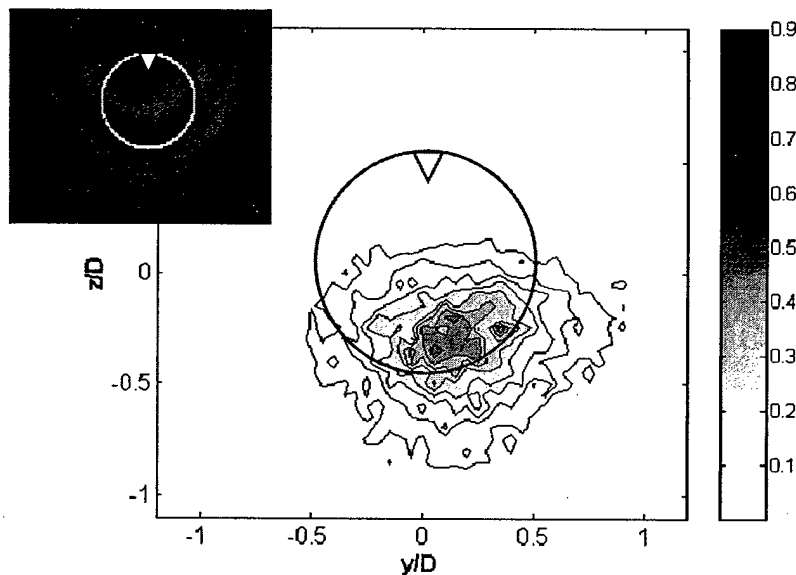


Figure 27: 2-D probability density distribution of apparent noise sources in the cross-stream plane for the single-tab jet.

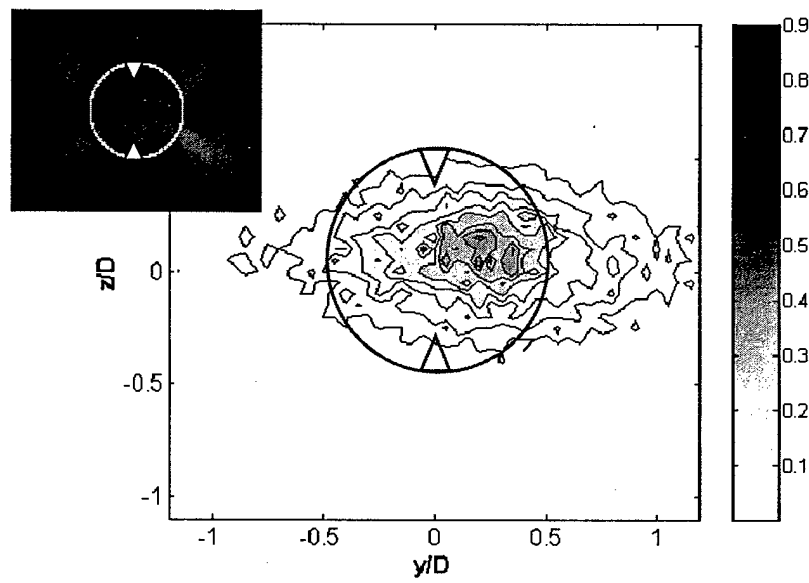


Figure 28: 2-D probability density distribution of apparent noise sources in the cross-stream plane for the dual-tab jet.

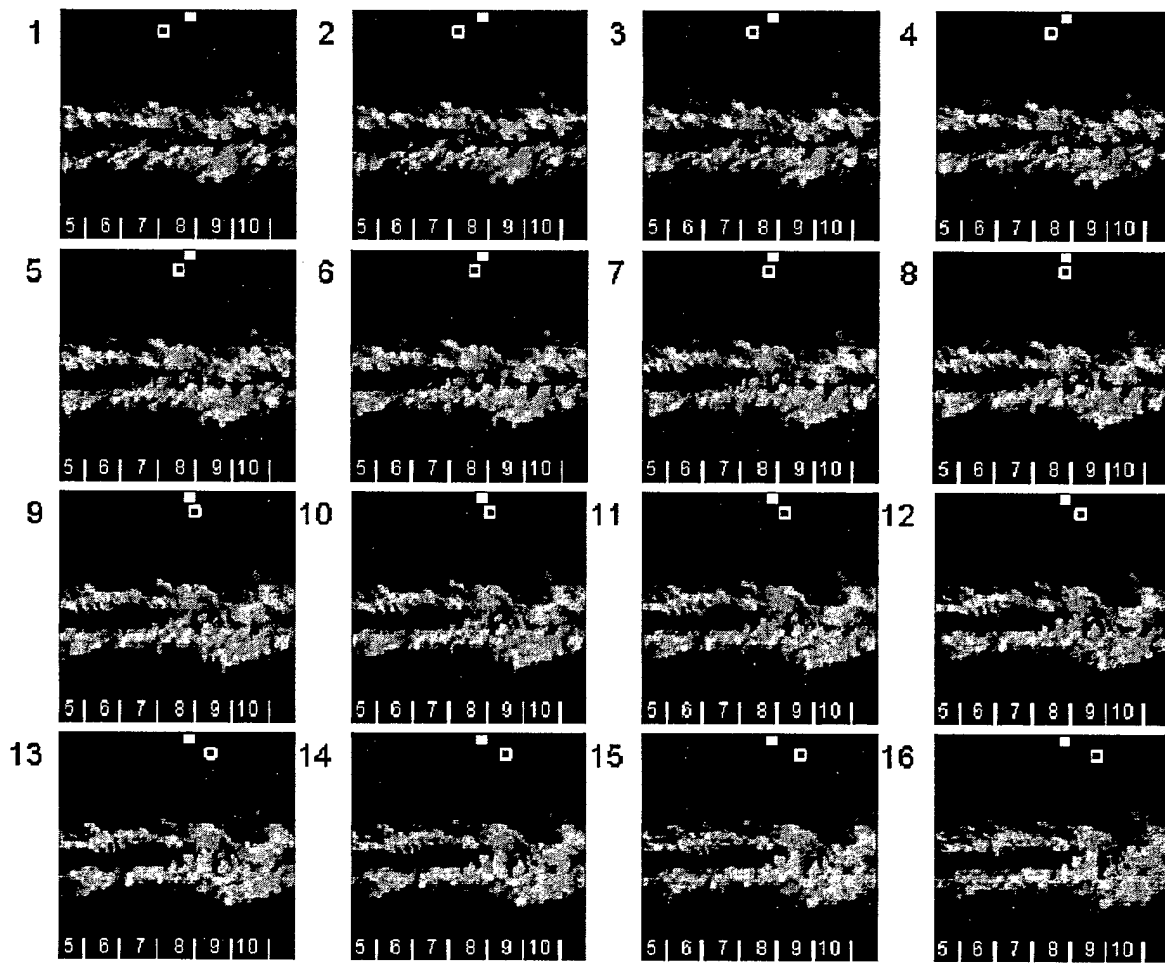


Figure 29: Example of an image set showing cross-mixing-layer interaction near the origin of an intense sound event.

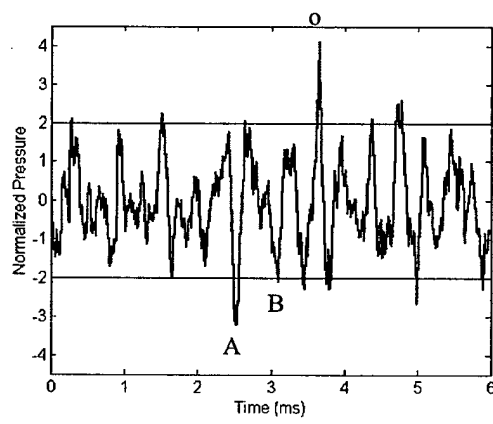


Figure 30: Far-field acoustic time signature corresponding to flow images of Figure 29. Time zero corresponds to the first laser pulse.

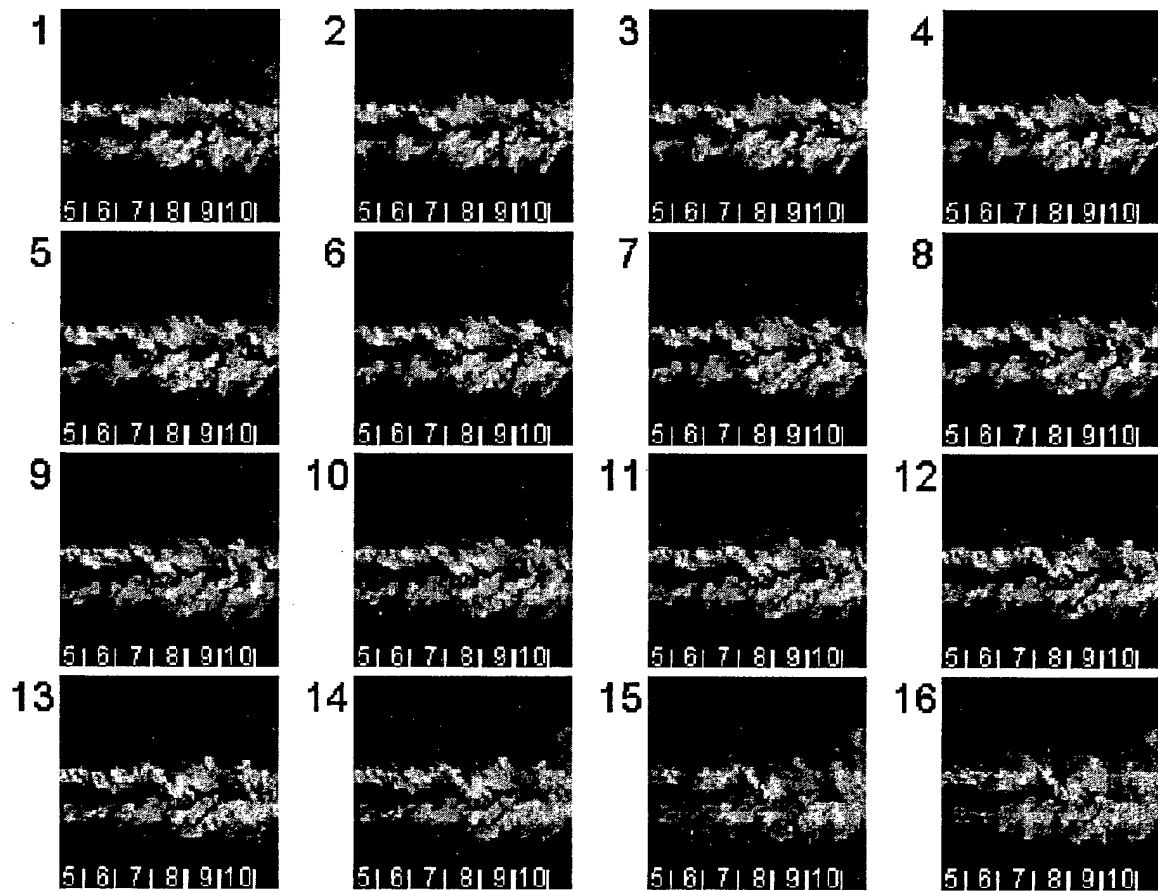


Figure 31: Example of an image set taken while the microphone array was recording a period of relative quiet.

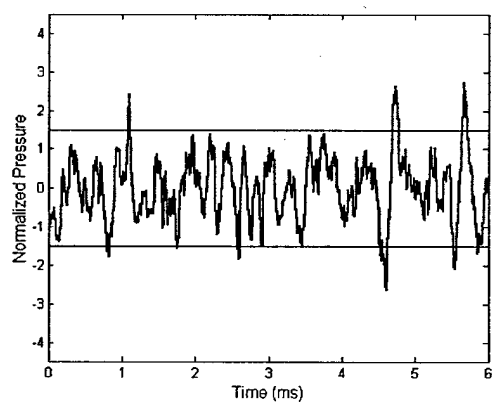


Figure 32: Far-field acoustic time signature corresponding to the flow images of Figure 31.

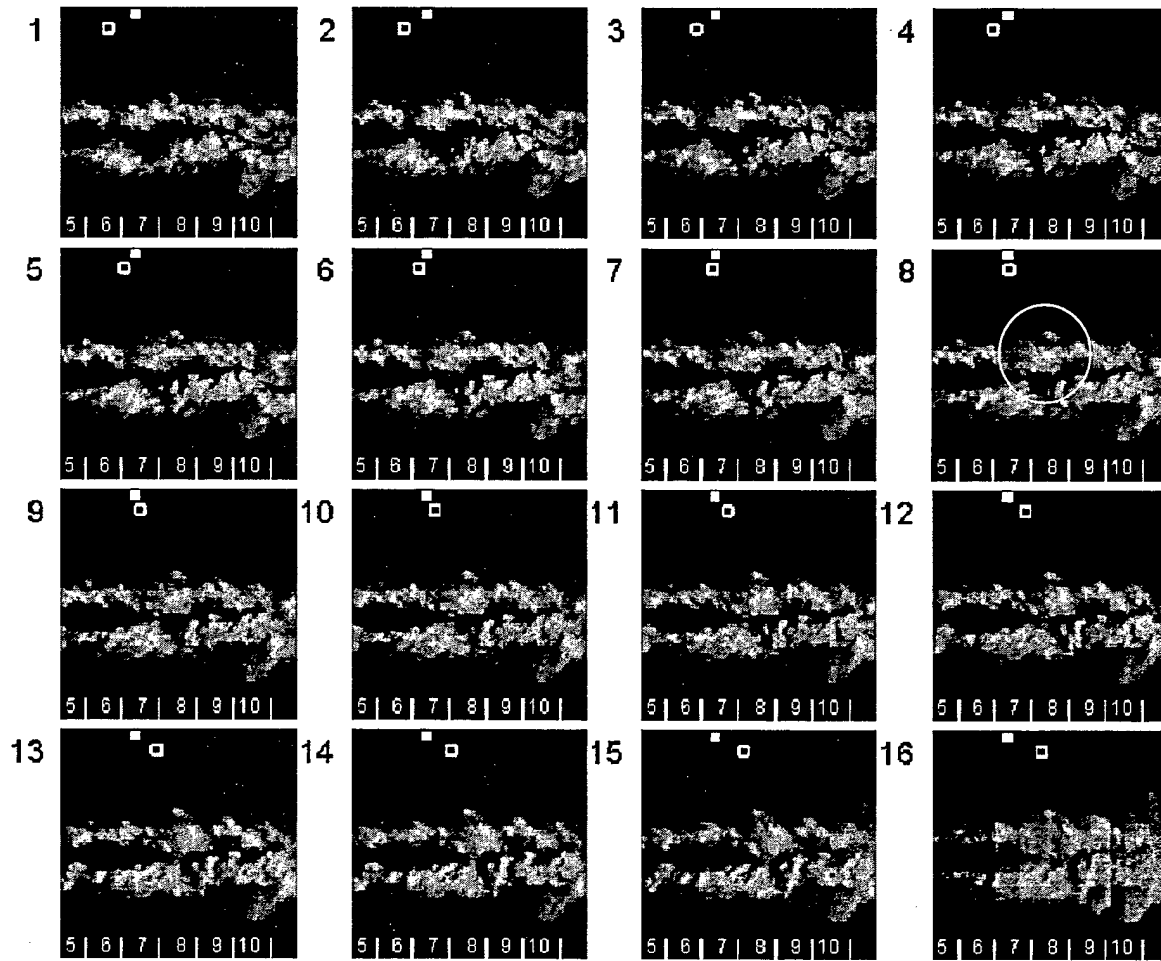


Figure 33: Example of an image set that shows structure roll-up near the origin of an intense sound event. The roll-up is circled in image 7.

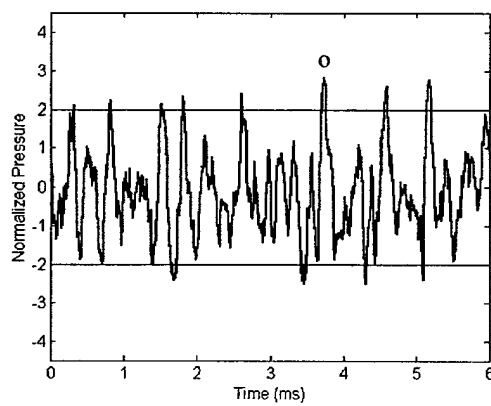


Figure 34: Far-field acoustic time signature corresponding to the flow images of Figure 33.

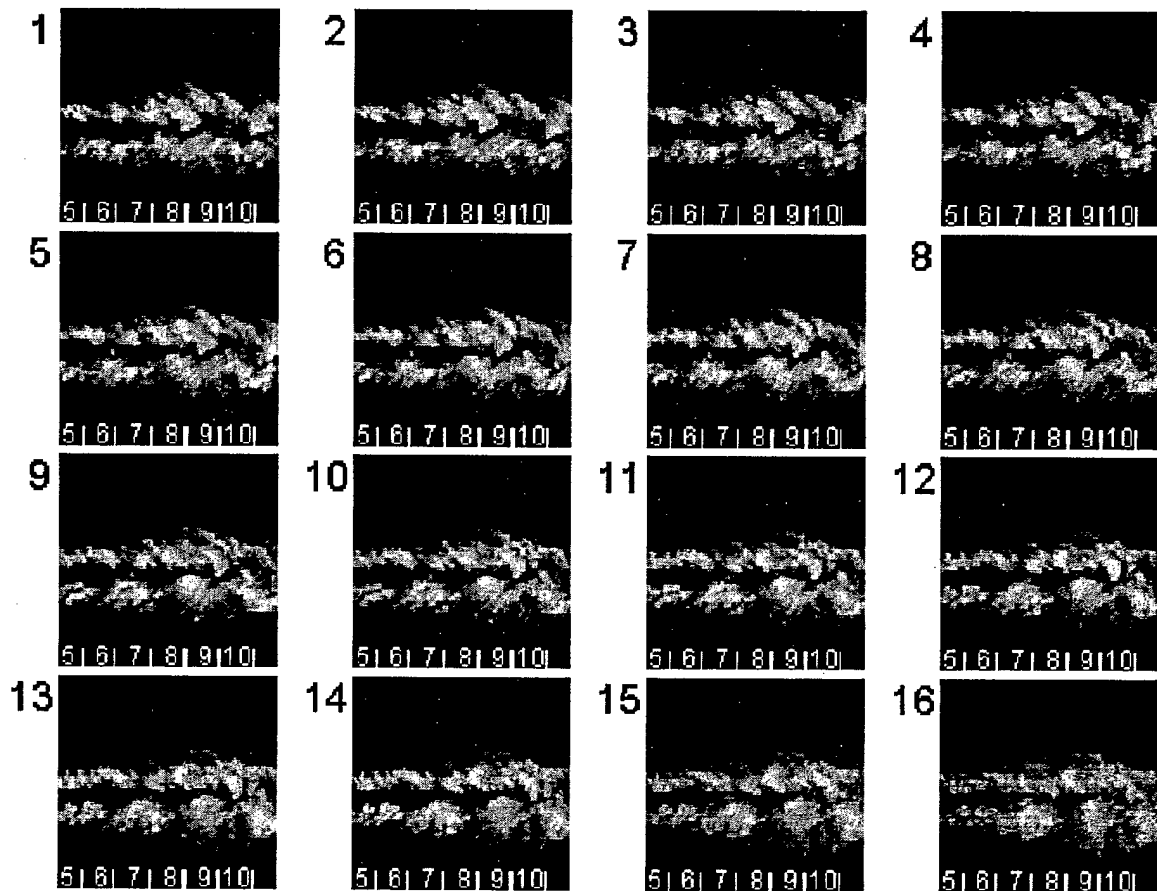


Figure 35: Example of an image set taken while the microphone array was recording a period of relative quiet.

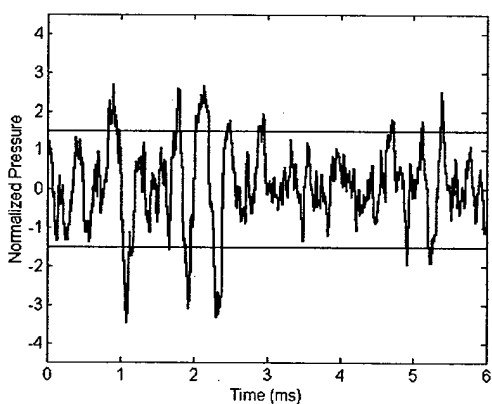


Figure 36: Far-field acoustic time signature corresponding to the flow images of Figure 35.

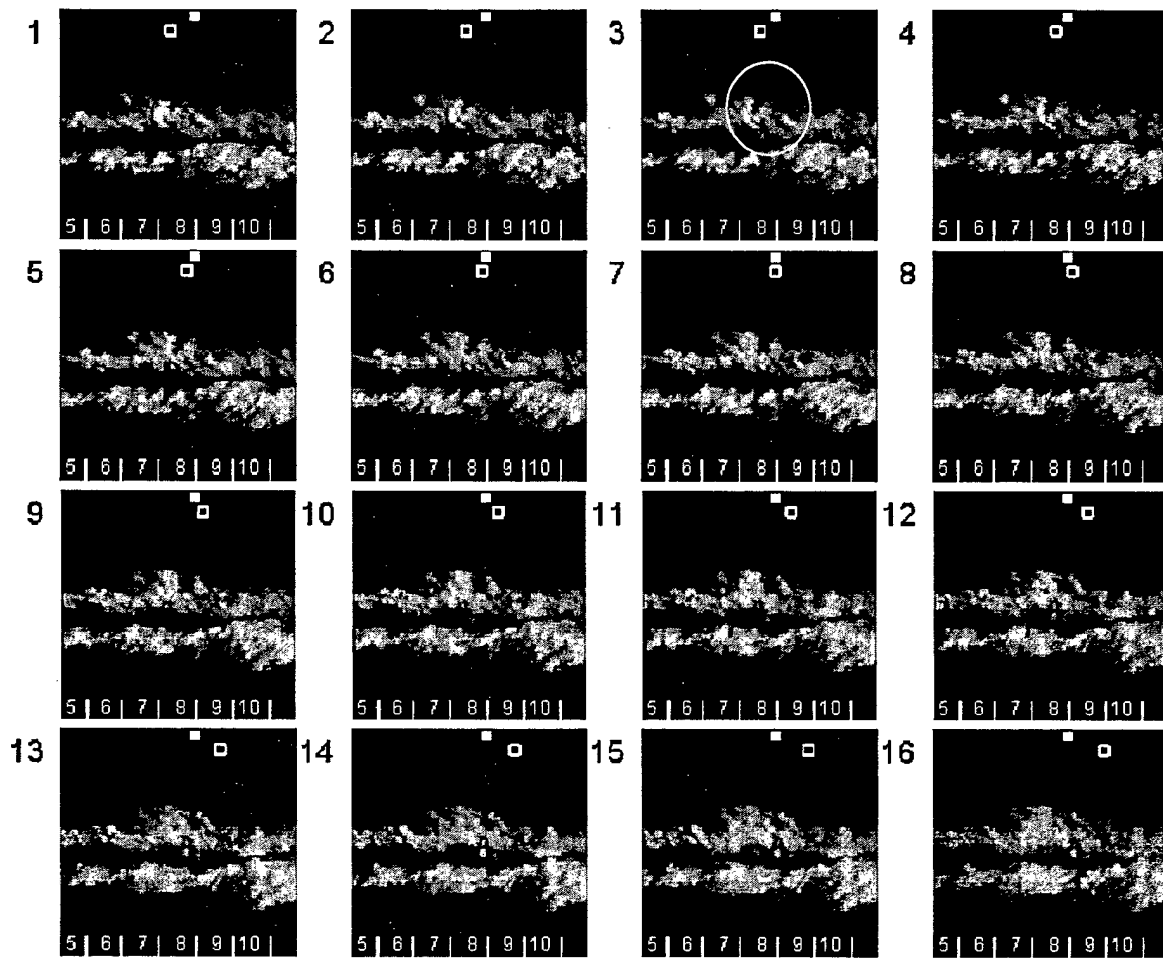


Figure 37: Example of an image set that shows structure tearing near the origin of an intense sound event. The region of tearing is circled in image 3.

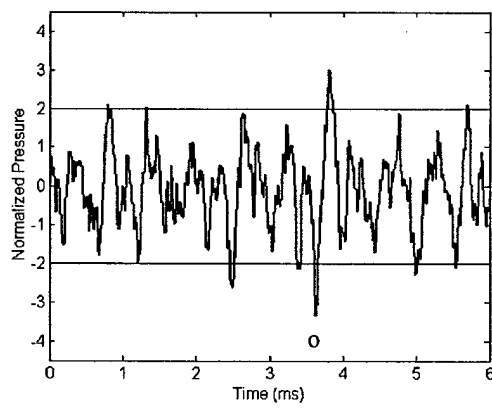


Figure 38: Far-field acoustic time signature corresponding to the flow images of Figure 37.

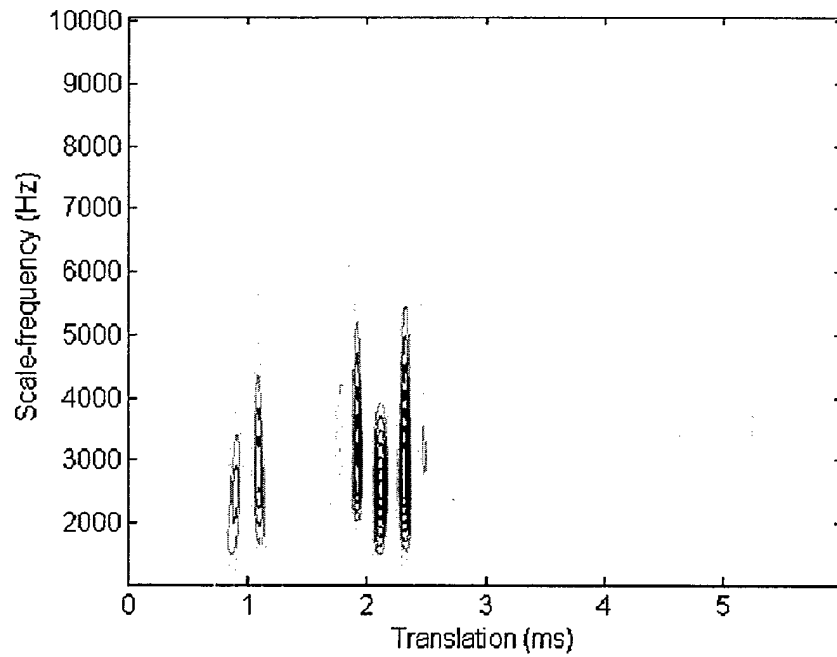


Figure 39: Energy distribution for the Mexican hat wavelet transformation of the time signature of Figure 36.

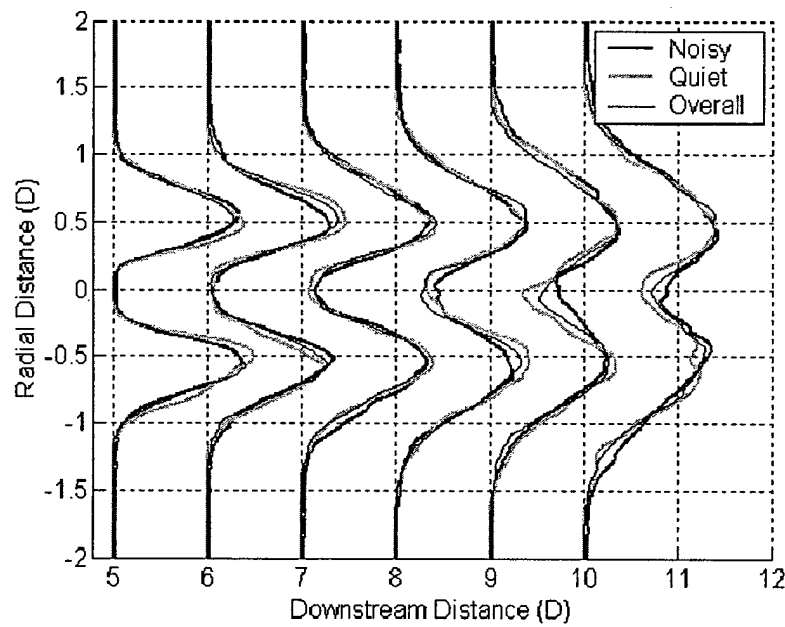


Figure 40: Plots of the average image intensity for the noise creation (noisy), relatively quiet (quiet), and random (overall) images at various downstream locations.

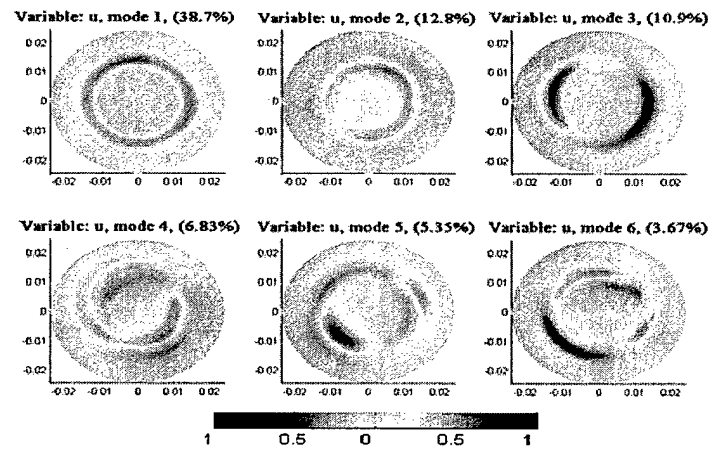


Figure 41: First 6 POD modes for the streamwise velocity fluctuations at $x/D=3$.

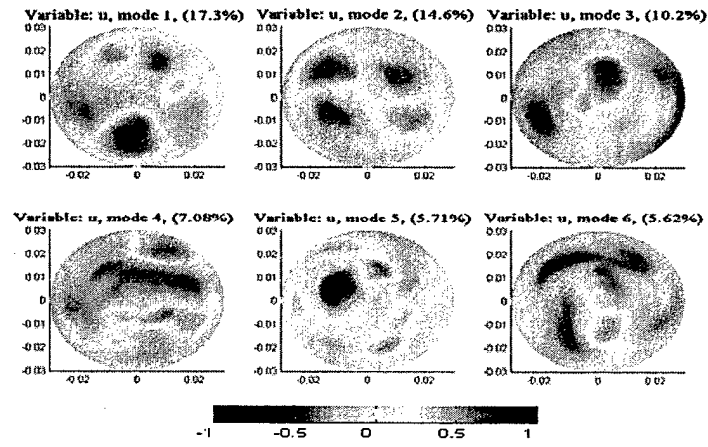


Figure 42: First 6 POD modes for the streamwise velocity fluctuations at $x/D=6$.

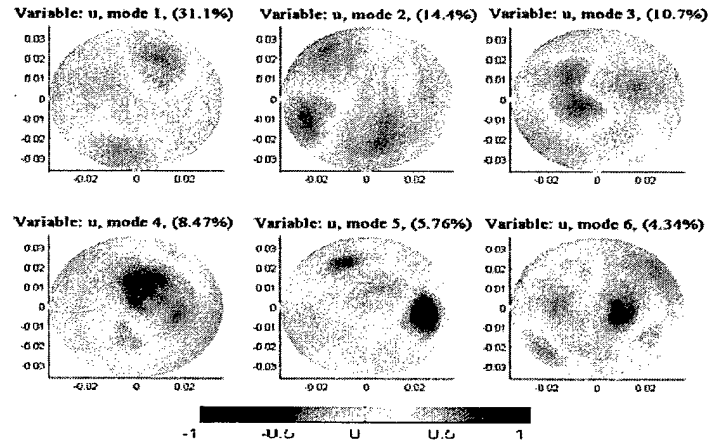


Figure 43: First 6 POD modes for the streamwise velocity fluctuations at $x/D=9$.

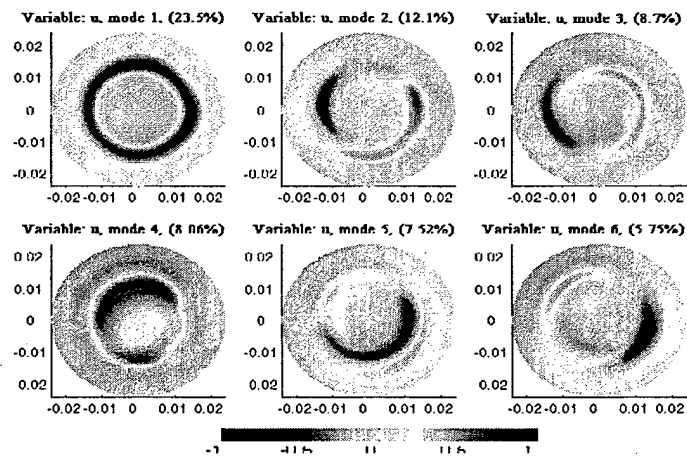


Figure 44: First 6 POD modes for the streamwise velocity fluctuations at $x/D=3$ using vector norm.

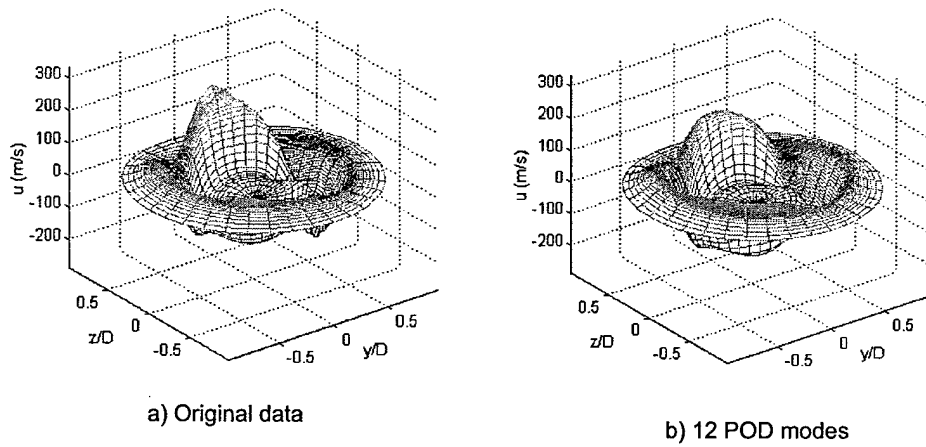


Figure 45: Instantaneous streamwise velocity fluctuations at $x/D = 3$, a) original field, b) reconstructed field using 12 POD modes

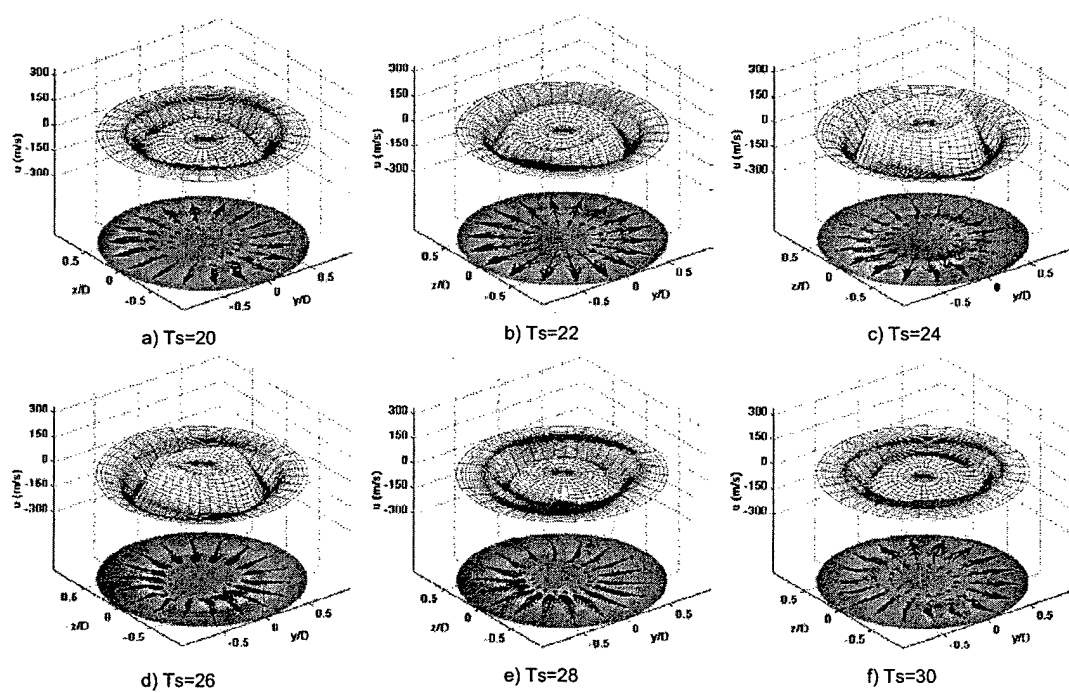


Figure 46: Three-dimensional reconstructions of the flow at different time steps using 12 POD modes showing the passage of an axisymmetric vortex ring: top image shows streamwise velocity fluctuations and bottom image shows combined cross-stream velocity vectors and streamwise vorticity contours.

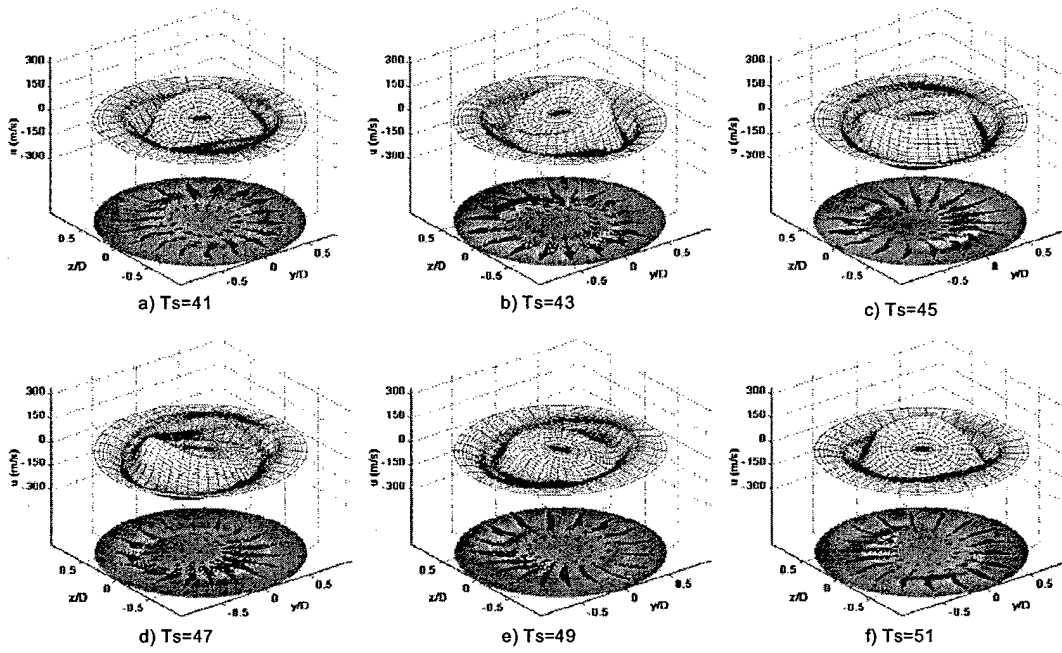


Figure 47: Three-dimensional reconstructions of the flow at different time steps using 12 POD modes showing the passage of an asymmetric structure (perhaps a helical structure): top image shows streamwise velocity fluctuations and bottom image shows combined cross-stream velocity vectors and streamwise vorticity contours.

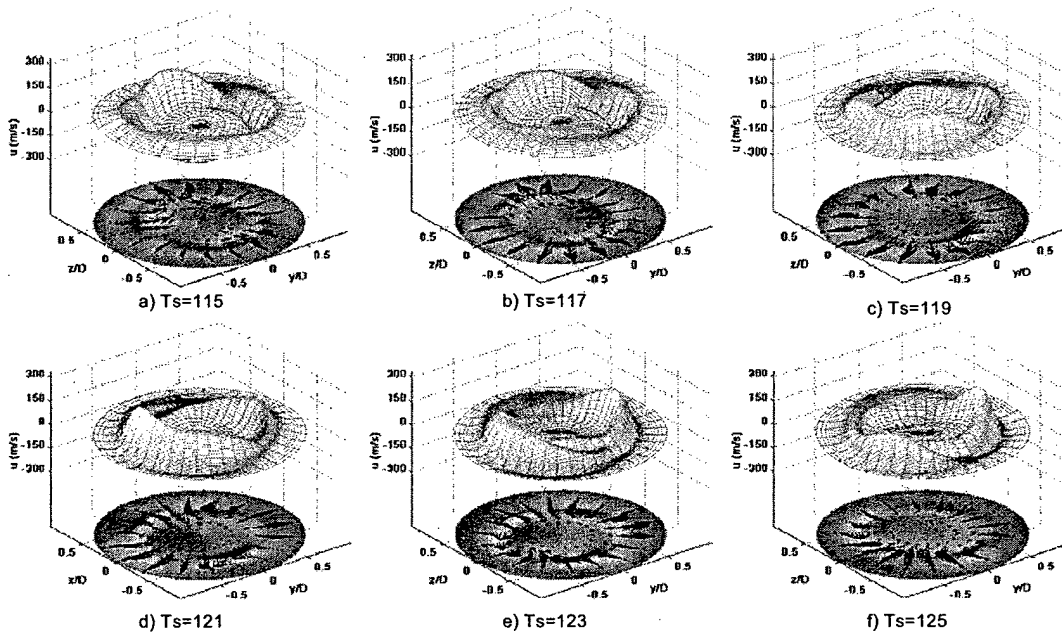


Figure 48: Three-dimensional reconstructions of the flow at different time steps using 12 POD modes showing the passage of a vortex pair: top image shows streamwise velocity fluctuations and bottom image shows combined cross-stream velocity vectors and streamwise vorticity contours.